Cell Reports

Article

Mosaic deletion of claudin-5 reveals rapid non-cell-autonomous consequences of blood-brain barrier leakage

Graphical abstract

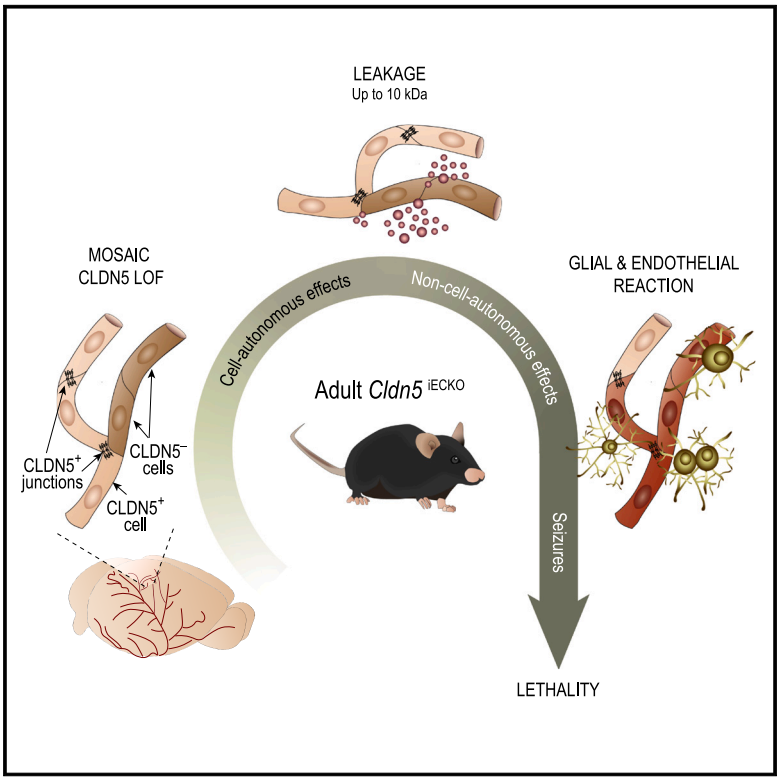

Highlights

- Cldn5 mosaic loss causes size-selective BBB permeability to tracers up to 10 kDa in size
- Adult-induced Cldn5 loss causes seizures and is lethal
- scRNA-seq excludes cell-autonomous transcriptional changes in endothelial cells
- Leakage causes endothelial and glial inflammation

Authors

Elisa Vázquez-Liébanas, Giuseppe Mocci, Weihan Li, ..., Matthew Campbell, Christer Betsholtz, Maarja Andaloussi Mäe

Correspondence

maarja.andaloussi_mae@igp.uu.se

In brief

Induced mosaic deletion of *Cldn5* in adult mice results in size-selective blood-brain barrier permeability and rapid death. Vázquez-Liébanas et al. show that, following CLDN5 loss, non-cell-autonomous changes appear in both the mutated and surrounding normal endothelial cells due to vascular leakage and ensuing brain inflammation.

Vázquez-Liébanas et al., 2024, Cell Reports *43*, 113911
March 26, 2024
https://doi.org/10.1016/j.celrep.2024.113911

CellPress

Cell Reports

CellPress
OPEN ACCESS

Article

Mosaic deletion of claudin-5 reveals rapid non-cell-autonomous consequences of blood-brain barrier leakage

Elisa Vázquez-Liébanas,[1] Giuseppe Mocci,[2] Weihan Li,[1] Bàrbara Laviña,[1,5] Avril Reddy,[3] Claire O'Connor,[3] Natalie Hudson,[3] Zaher Elbeck,[1] Ioannis Nikoloudis,[1] Konstantin Gaengel,[1] Michael Vanlandewijck,[1,2,4] Matthew Campbell,[3] Christer Betsholtz,[1,4] and Maarja Andaloussi Mäe[1,6,*]

[1]Department of Immunology, Genetics, and Pathology, Rudbeck Laboratory, Uppsala University, 751 85 Uppsala, Sweden
[2]Single Cell Core Facility of Flemingsberg Campus (SICOF), Karolinska Institute, 14157 Huddinge, Sweden
[3]Smurfit Institute of Genetics, Trinity College Dublin, Dublin 2, Ireland
[4]Department of Medicine, Karolinska Institute, 14157 Huddinge, Sweden
[5]Present address: Department of Clinical Pathology, Akademiska Sjukhuset, 751 85 Uppsala, Sweden
[6]Lead contact
*Correspondence: maarja.andaloussi_mae@igp.uu.se
https://doi.org/10.1016/j.celrep.2024.113911

SUMMARY

Claudin-5 (CLDN5) is an endothelial tight junction protein essential for blood-brain barrier (BBB) formation. Abnormal CLDN5 expression is common in brain disease, and knockdown of Cldn5 at the BBB has been proposed to facilitate drug delivery to the brain. To study the consequences of CLDN5 loss in the mature brain, we induced mosaic endothelial-specific *Cldn5* gene ablation in adult mice (*Cldn5*^{iECKO}). These mice displayed increased BBB permeability to tracers up to 10 kDa in size from 6 days post induction (dpi) and ensuing lethality from 10 dpi. Single-cell RNA sequencing at 11 dpi revealed profound transcriptomic differences in brain endothelial cells regardless of their *Cldn5* status in mosaic mice, suggesting major non-cell-autonomous responses. Reactive microglia and astrocytes suggested rapid cellular responses to BBB leakage. Our study demonstrates a critical role for CLDN5 in the adult BBB and provides molecular insight into the consequences and risks associated with CLDN5 inhibition.

INTRODUCTION

The endothelial lining of the blood vasculature forms the primary interface for molecular and cellular exchange between the blood and tissue parenchyma. In the brain of most vertebrates, including mammals, the vascular endothelium harbors an organotypic specialization known as the blood-brain barrier (BBB), essential to secure a constant milieu optimal for neuronal and glial functions. This specialization encompasses tight endothelial adhesion, low endothelial transcellular vesicular transport, and a multitude of endothelial cell membrane-bound transporters that promote influx of necessary nutrients and efflux of metabolic waste products and prevent potentially neurotoxic substances present in the blood from entering into the brain parenchyma.[1,2] Similar to the epithelial barriers present in many different organs, the BBB depends on specialized intercellular junctions, including tight junctions. In endothelial cells, tight junctions are located close to the apical (luminal) membrane of endothelial cells. Claudin-5 (CLDN5) is the most abundant tight junction protein in endothelial cells and is particularly highly expressed in central nervous system (CNS) endothelial cells.[3] The CLDN5 protein is encoded by a single exon in mice (two exons in humans) and consists of four transmembrane domains, two extracellular loops (ECLs), a short intracellular loop, a short amino terminus, and a longer carboxylic terminus.[4,5] Classical claudins, such as CLDN5, hold conserved motifs at the ECLs that control paracellular tightness via formation of *cis* and *trans* interactions.[5–10] In the cytoplasm, the carboxylic tail contains phosphorylation sites controlling recycling and degradation of the protein and a PDZ (post synaptic density protein [PSD95], Drosophila disc large tumor suppressor [DLG1], and zonula occludens-1 protein [ZO1]) domain important for scaffold protein binding and subsequent anchorage to the cytoskeleton.[11–14] In the brain, CLDN5 interacts with the scaffold proteins ZO1 and ZO2.[4,14,15]

CLDN5 is essential for the development of a functional BBB. Constitutive deletion of the *Cldn5* gene in mice was reported to cause size-selective BBB permeability for molecules up to 742 Da in size and early postnatal death.[16] In zebrafish, one of the two *cldn5* homologs, *cldn5a*, is expressed in both the BBB and in choroid plexus epithelial cells in the blood-cerebrospinal fluid barrier (BCFB) and *cldn5a*−/− zebrafish showed increased lethality and permeability across the BBB and or BCFB for tracers up to 10 kDa in size.[17] Changes in the expression of the Cldn5 mRNA and protein have been reported in several brain

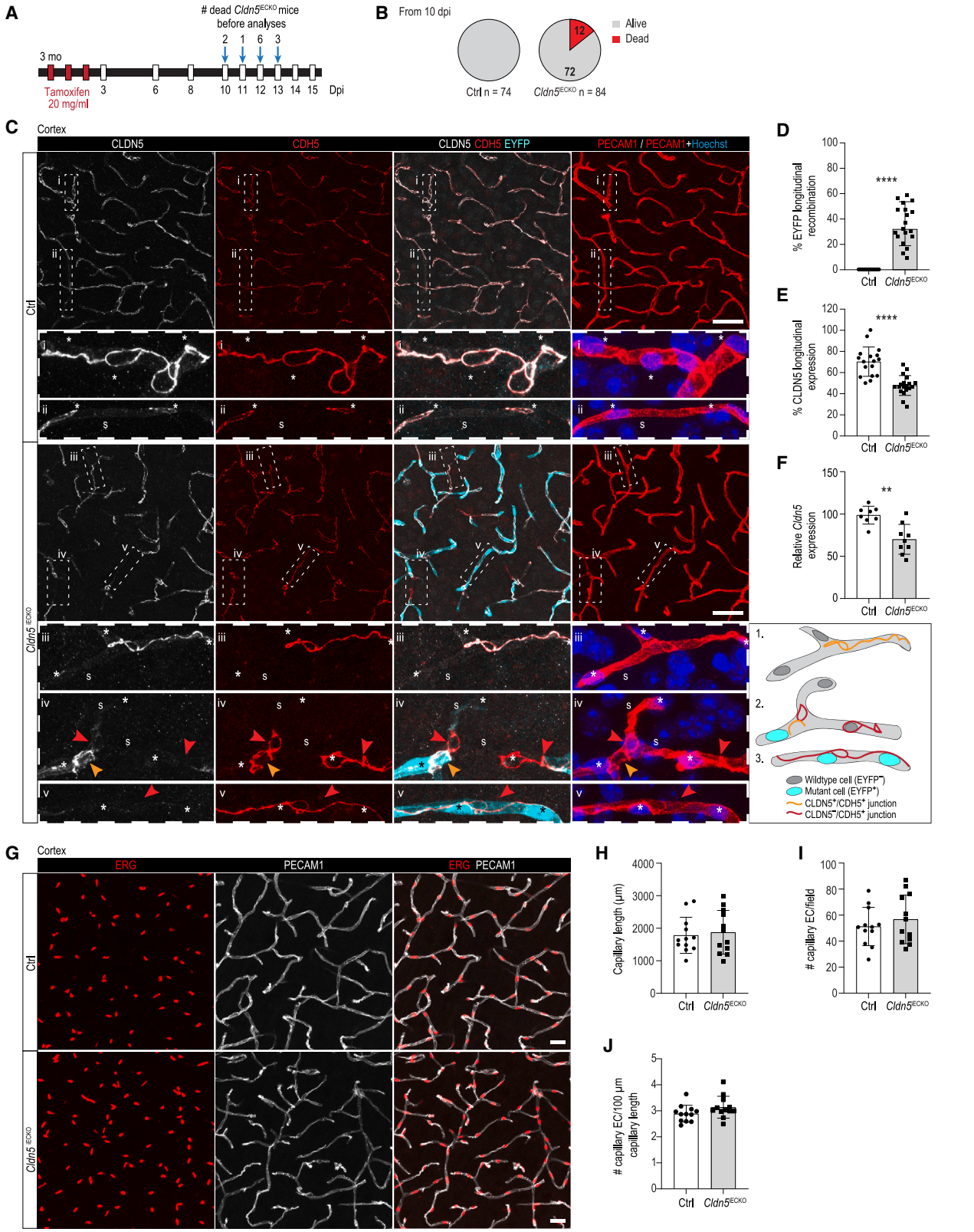

(legend on next page)

diseases in humans, as well as in mouse models of neurovascular dysfunction. Cldn5 (mRNA and/or protein) expression is reduced considerably in mice 2 days after acute ischemic stroke in the stroke core region.[18] Decrease in Cldn5 expression and increased BBB permeability has also been reported in *Unc5b* knockout (KO)[19] and pericyte-deficient mouse models.[20] In humans, early stages of multiple sclerosis (MS) exhibit BBB disruption with redistribution of junctional proteins, including CLDN5.[21] Decreased Cldn5 levels have also been reported in treatment-resistant epilepsy patient brains[22] and in individuals with schizophrenia and depression.[23–25] It is, however, unclear if Cldn5 dysregulation contributes causally to these pathologies or whether it is a consequence without pathogenic importance. In spite of this uncertainty, CLDN5-targeted BBB opening is actively investigated for small-molecule drug delivery into brain.[26] However, a deeper understanding of the safety aspect of this type of on-demand BBB opening is currently missing.

The goal of this study was to investigate the physiological importance of CLDN5 in the healthy adult brain and the potential pathological consequences of its deletion from brain endothelial cells. To achieve this, we induced endothelial-specific *Cldn5* KO in 3-month-old mice (*Cldn5*^{iECKO}), which resulted in mosaic loss of CLDN5 in brain endothelial cells, increased size-selective BBB permeability to exogenous tracers from 6 days post induction (dpi) and ensuing lethality from 10 dpi. The single-exon structure of *Cldn5* combined with its high expression in brain endothelial cells allowed us to distinguish *Cldn5*-negative (*Cldn5*$^{-}$) from *Cldn5*-positive (*Cldn5*$^{+}$) endothelial cells in mosaic *Cldn5*^{iECKO} mouse brains by single-cell RNA sequencing (scRNA-seq). This revealed extensive but highly similar transcriptional changes in *Cldn5*$^{-}$ and *Cldn5*$^{+}$ cells in mosaic *Cldn5*^{iECKO} mice, suggesting profound non-cell-autonomous endothelial responses. In addition, *Cldn5*^{iECKO} brains displayed ample signs of endothelial and glial cell inflammation, suggesting that BBB opening by tight junction disruption rapidly engages multiple cell types of the CNS innate immune system with deleterious consequences for brain function.

RESULTS

Cldn5 deletion timeline and lethality in adult Cldn5^{iECKO} mice

In order to delete *Cldn5* in the endothelium of adult mice, *Cldn5*$^{Flox/Flox}$ mice (Figure S1A) were crossed with tamoxifen-inducible *Cdh5*-Cre ERT2 (Cre) mice[27] to generate inducible endothelial-specific *Cldn5* KO mice (*Cldn5*^{iECKO}) of both sexes. Tamoxifen-treated Cre-negative *Cldn5*$^{Flox/Flox}$ littermates were used as controls (Ctrl) in all experiments. Both *Cldn5*^{iECKO} and Ctrl mice carried the reporter transgene *Rosa26*$^{EYFP/EYFP}$ (*Rosa26*-EYFP reporter)[28] to aid the evaluation of Cre recombination efficiency.[29] Two milligrams of tamoxifen was administered on three consecutive days to 3-month-old mice, which were subsequently analyzed at 3–15 days after the first tamoxifen dose (dpi). A total of 87 Ctrl and 99 *Cldn5*^{iECKO} mice were generated for analysis. However, from 10 dpi, *Cldn5*^{iECKO} mice began to die (Figure 1A), and 14% of *Cldn5*^{iECKO} mice were found dead before the analysis, most of them at 12 or 13 dpi (Figures 1A and 1B). In two litters, the *Cldn5*^{iECKO} mice displayed particularly severe phenotypes. In one of the litters, consisting of five Ctrl and five *Cldn5*^{iECKO} mice, behavior was observed twice daily following tamoxifen administration. Among the *Cldn5*^{iECKO} mice, one suffered severe seizures at 11 dpi, a second was found dead at 12 dpi, and the remaining three appeared distressed and/or had balance issues commencing at 11–13 dpi. All five tamoxifen-treated Ctrl mice behaved normally with no signs of distress. The second litter was sacrificed for analysis at 15 dpi. In all experiments, individual mice were sacrificed for tissue analyses as soon as possible after onset of symptoms.

For immunofluorescence tissue analysis, mice were perfusion fixed and their brains dissected and sectioned. In agreement with the findings previously reported for constitutive *Cldn5* KOs,[16] we did not find any apparent differences between Ctrl and *Cldn5*^{iECKO} mice analyzed at 11 dpi in the distribution of adherens junction (CDH5, PECAM1) or tight junction proteins (OCLN, ZO1) other than CLDN5 itself (Figures S1B and S1C).

Figure 1. Claudin-5 mosaic deletion and lethality in adult-induced *Cldn5*^{iECKO} mice

(A) Number of dead *Cldn5*^{iECKO} mice before analyses at 3–15 days post induction (dpi).

(B) Number of analyzed mice from 10 to 15 dpi and proportion of dead and alive mice in each genotype is illustrated.

(C) Representative images of the immunostainings of adult mouse brain cortex at 11 dpi showing the tight junction protein CLDN5, the adherens junction proteins CDH5, the reporter EYFP, and PECAM1. Scale bars, 50 μm. (i) A stretch of the control endothelium with CLDN5^{+} tight junctions. (ii) A seamless (S) junction in the control endothelium. (iii) A stretch of the *Cldn5*^{iECKO} endothelium with CLDN5^{+} tight junctions and no EYFP expression. (iv) A stretch of the *Cldn5*^{iECKO} endothelium partly devoid of CLDN5 tight junctions where EYFP^{+} cells are next to EYFP^{-} cell. Red arrowheads show CLDN5^{-}/CDH5^{+} junctions, while the orange arrowhead shows a CLDN5^{+}/CDH5^{+} junction in between wild-type and KO cells. (v) A stretch of the *Cldn5*^{iECKO} endothelium devoid of CLDN5 where two EYFP+ cells are next to each other. Cartoon illustrates the three alternating/mosaic cellular patterns of loss of CLDN5 and activation of EYFP in *Cldn5*^{iECKO} endothelium. Asterisk (*) marks endothelial cell nucleus. S, seamless junction.

(D) %EYFP longitudinal recombination in the capillaries relative to PECAM1 length.

(E) %CLDN5 longitudinal expression relative to PECAM1 length in the capillaries. For (D) and (E), the mice were analyzed at 11 dpi (four litters, Ctrl n = 12, *Cldn5*^{iECKO} n = 13), 14 dpi (n = 3), and severe litter (Ctrl n = 2, *Cldn5*^{iECKO} n = 3).

(F) Microvascular fragment isolation and qPCR analysis from fresh cerebrums. Two litters, 11 dpi (n = 4), 12 dpi (Ctrl n = 2, *Cldn5*^{iECKO} n = 3), and 13 dpi (Ctrl n = 2, *Cldn5*^{iECKO} n = 3).

(G) Representative images from the cortex of *Cldn5*^{iECKO} and Ctrl. PECAM1, endothelium; ERG, endothelial cell nuclei. Scale bars, 25 μm.

(H) Quantification of capillary length via PECAM1 staining.

(I) Quantification of ERG^{+} endothelial cell numbers in capillaries per field.

(J) Quantification of endothelial cell numbers per 100 μm of capillary length per field. For (H)–(J), the mice were analyzed at 11 dpi (two litters, n = 12) and severe litter (Ctrl n = 2, *Cldn5*^{iECKO} n = 3). (D, E, and I) The data were not normally distributed so nonparametric Mann-Whitney U test was used to evaluate significance. (F, H, and J) The significance of normally distributed data was evaluated using unpaired two-tailed t test with Welch's correction. Data are presented as geometric mean with geometric SD, except for (D), where data are presented as mean ± SD. **p < 0.01, ****p < 0.0001. See also Figure S1.

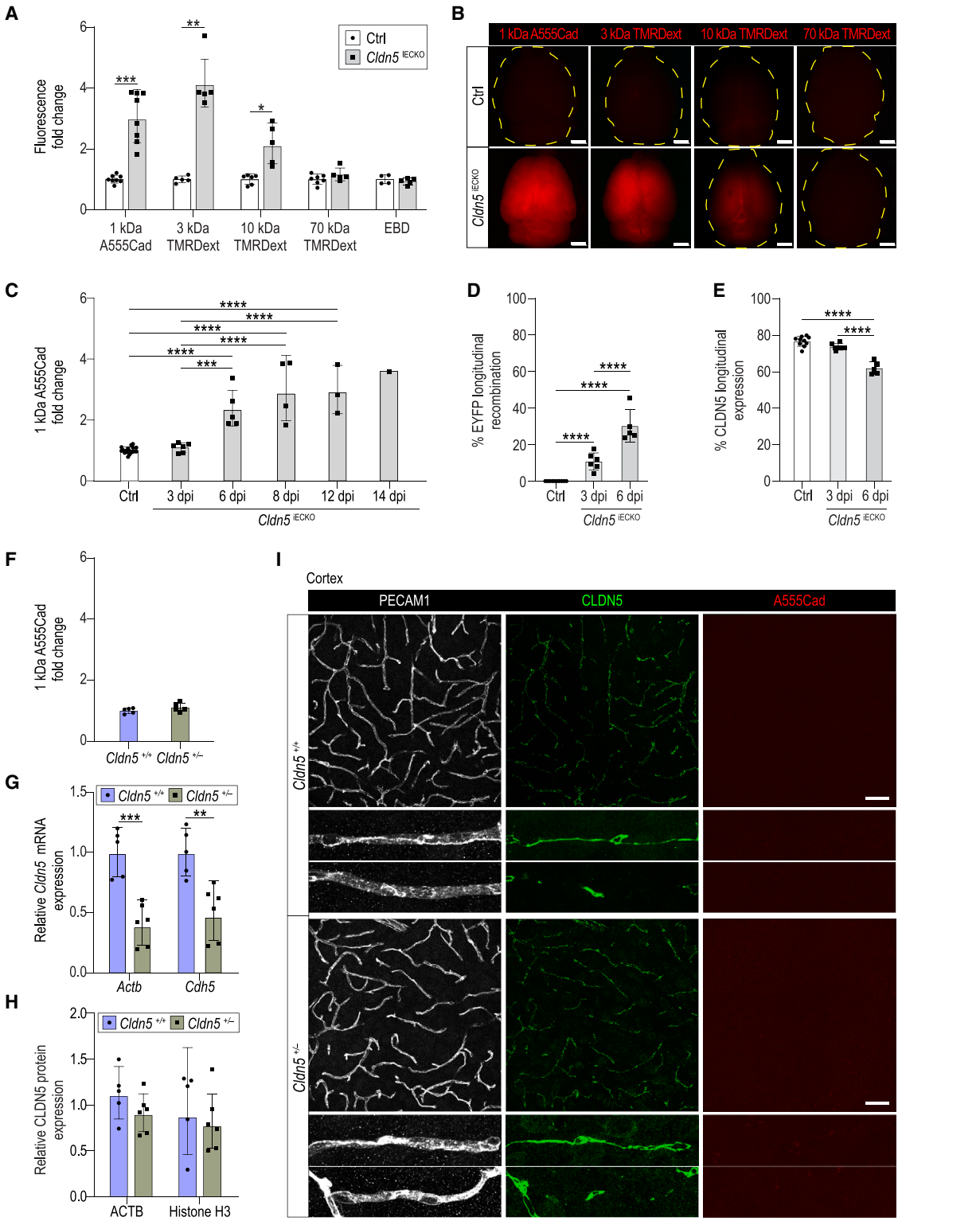

Figure 2. Assessment of BBB integrity in adult-induced *Cldn5*^{iECKO} and *Cldn5*$^{+/-}$ mice

(A) Quantification of relative fluorescence of tracers at 8–14 dpi: 1-kDa A555-Cadaverine (A555Cad) (three litters, n = 8), 3 kDa (two litters, n = 5), 10-kDa TMR-dextran (two litters, Ctrl n = 6, *Cldn5*^{iECKO} n = 5) after 2-h circulation, and 70-kDa TMR-dextran (two litters, Ctrl n = 7, *Cldn5*^{iECKO} n = 5) and Evans blue dye (EBD) (Ctrl n = 4, *Cldn5*^{iECKO} n = 5) after overnight circulation. Results are shown as fold change of the Ctrl average values.

(B) Representative images of the brains of mice after tracer administration and perfusion. Dotted yellow lines mark the outline of the brains. Scale bars, 2 mm.

(legend continued on next page)

To assess *Cldn5* gene deletion efficiency, immunostainings of CLDN5, CDH5, EYFP, and PECAM1 were performed on brain sections from 11 dpi Ctrl and *Cldn5*^{iECKO} mice (Figure 1C). In the cortex, all endothelial cells in Ctrl brains showed CLDN5^{+} stretches of cell contacts overlapping with the CDH5 expression pattern (Figure 1C). Occasional capillary stretches that were PECAM1^{+} and CLDN5 negative ($^{-}$) were also CDH5^{-}, probably representing cells without auto-cellular junctions, i.e., "seamless" tubes.[30,31] *Cldn5*^{iECKO} endothelium displayed three alternating/mosaic cellular patterns of loss of CLDN5 and activation of EYFP. First, CLDN5^{+}/CDH5^{+} junctions were observed at contacts between neighboring EYFP^{-} (presumably wild-type) cells similar to the situation in Ctrl mice (Figure 1C). Second, CLDN5$^{low/-}$/CDH5^{+} junctions were observed at contacts between EYFP^{+} (presumably mutant) and EYFP^{-} (presumably wild-type) cells (Figure 1C). Third, CLDN5^{-}/CDH5^{+} junctions were observed between neighboring EYFP^{+} (presumably mutant) cells (Figure 1C).

To quantify the extent of *Cldn5* deletion in the *Cldn5*^{iECKO} mice at 11–15 dpi, we used three approaches: (1) *Rosa26*-EYFP reporter activation, which correlated well with CLDN5 loss at the cellular level in spite of being independent Cre-mediated recombination events; (2) comparison between the longitudinal labeling of CLDN5 and PECAM1 in capillaries; and (3) the relative *Cldn5* mRNA expression assessed by quantitative (q)PCR in microvascular fragments (MVFs) isolated from cerebrum (Figures 1D–1F, respectively). By approach (1), we found ~35% of the brain capillary length EYFP^{+} in *Cldn5*^{iECKO} brain cortex (Figure 1D) and similar values were found also in hippocampus and thalamus (Figures S1D and S1E). By approach (2), we found that the CLDN5 longitudinal expression over PECAM1 was reduced by ~33% in *Cldn5*^{iECKO} capillaries compared to Ctrl (Figure 1E), irrespective of brain regions (Figures S1D and S1F). Approach (3) revealed an average 36% reduction in *Cldn5* mRNA compared to Ctrl (Figure 1F). In conclusion, all three methods indicated a similar average level of CLDN5 mosaic deletion in our experiment, approximately 35%.

The general vascular morphology in *Cldn5*^{iECKO} mouse cerebral cortex at 11–15 dpi (Figure 1G) was not significantly different from Ctrl in terms of PECAM1^{+} capillary length (Figures 1G and 1H), number of capillary endothelial cells (ERG^{+}) per field (Figures 1G and 1I), or number of capillary endothelial cells per 100 μm of capillary vessel length (Figures 1G and 1J).

Size-selective BBB permeability timeline in adult Cldn5^{iECKO} brain

Complete loss of *Cldn5* during development or transient downregulation of *Cldn5* in adult mice were both reported to cause increased paracellular leakage of molecules from the blood to the brain in a size-selective manner, with molecules up to 742 Da crossing the BBB.[16,32] To investigate BBB leakage characteristics following adult-induced mosaic *Cldn5* KO, we injected different sizes of fluorescently labeled tracers (1, 3, 10, and 70 kDa) and Evans blue dye (EBD, size 69.96 kDa when bound to albumin) (Table S1) into the tail vein at 8–14 dpi. The tracers were left to circulate for 2–16 h (Table S1) before perfusion with Hank's Balanced Salt Solution (HBSS). Brains and kidneys were homogenized and the relative fluorescence of extravasated tracers was quantified. While tracers up to 10 kDa in size showed significant leakage into the brain parenchyma of *Cldn5*^{iECKO} mice, neither 70-kDa tetramethylrhodamine (TMR)-dextran nor albumin-bound EBD were measurably increased (Figures 2A and 2B). Tracer accumulation in the kidneys was similar in *Cldn5*^{iECKO} and Ctrl (Figures S2A and S2B), arguing against systemic changes in vascular permeability. Immunostainings of brain vibratome sections from *Cldn5*^{iECKO} mice injected with 1-kDa Alexa Fluor 555-Cadaverine (A555Cad) showed tracer uptake by NEUN^{+} neurons (Figure S2C), as previously reported for pericyte-deficient mice with BBB impairment.[33]

Because seizures and death were observed from 10 dpi, we were interested to know if Cldn5 deletion was progressive between the first tamoxifen injection (0 dpi) and symptom onset (10 dpi). We therefore addressed the time course of tracer leakage and CLDN5 elimination following tamoxifen administration. We found that leakage of A555Cad increased specifically in *Cldn5*^{iECKO} brains from 6 dpi and onwards (Figure 2C), whereas there was no significant difference in A555Cad accumulation in kidneys between Ctrl and *Cldn5*^{iECKO} at any studied time points (Figure S2D). Using EYFP^{+} as surrogate for *Cldn5* KO (approach (1), see above), we found that ~11% of the cerebral cortex capillary length was EYFP^{+} in *Cldn5*^{iECKO} brains at 3 dpi, which increased to ~30% at 6 dpi (Figure 2D). A similar time course was observed for CLDN5 longitudinal expression over

(C) Quantification of relative fluorescence of 1-kDa A555Cad after 2-h circulation, presented as fold change over Ctrl. The quantifications were made at 3 dpi (two litters, n = 6), 6 dpi (two litters, Ctrl n = 4, *Cldn5*^{iECKO} n = 5), 8 dpi (Ctrl n = 3, *Cldn5*^{iECKO} n = 4), 12 dpi (n = 3), and 14 dpi (Ctrl n = 2, *Cldn5*^{iECKO} n = 1). The quantifications for 8, 12, and 14 dpi were taken from (A). The Ctrl datapoints from each dpi were merged into one bar.
(D) %EYFP longitudinal recombination in the capillaries relative to PECAM1 length at 3 and 6 dpi.
(E) %CLDN5 longitudinal expression relative to PECAM1 length in the capillaries at 3 and 6 dpi.
(F) Quantification of relative fluorescence of 1-kDa A555Cad after 2-h circulation in adult *Cldn5*$^{+/+}$ and *Cldn5*$^{+/-}$ mouse brains. Results are shown as fold change of the *Cldn5*$^{+/+}$ average values (two litters, n = 5).
(G) qPCR analysis of microvascular fragments isolated from *Cldn5*$^{+/+}$ and *Cldn5*$^{+/-}$ cerebrums. *Cldn5* mRNA expression was normalized to *Actb* and *Cdh5* (two litters, *Cldn5*$^{+/+}$ n = 5, *Cldn5*$^{+/-}$ n = 6).
(H) Western blot analysis of microvascular fragment isolated *Cldn5*$^{+/+}$ and *Cldn5*$^{+/-}$ cerebrums. CLDN5 expression was normalized to ACTB and histone H3 (two litters, *Cldn5*$^{+/+}$ n = 5, *Cldn5*$^{+/-}$ n = 6).
(I) Representative images of the brain immunostainings of adult *Cldn5*$^{+/+}$ and *Cldn5*$^{+/-}$ mice (n = 5) after 1-kDa A555Cad administration and perfusion. Scale bars, 25 μm. (A) For 3- and 10-kDa TMR-dextran, the data were not normally distributed so nonparametric Mann-Whitney U test was used to evaluate significance. In (A; A555Cad, 70 kDa TMR-dextran, and EBD) and (F–H) the significance of normally distributed data was evaluated using unpaired two-tailed t test with Welch's correction. (C, D, and E) Data were normally distributed and significance of data was evaluated using Tukey's multiple comparisons test. Data are presented as geometric mean with geometric SD. *p < 0.05, **p < 0.01, ***p < 0.001, ****p < 0.0001. See also Figure S2.

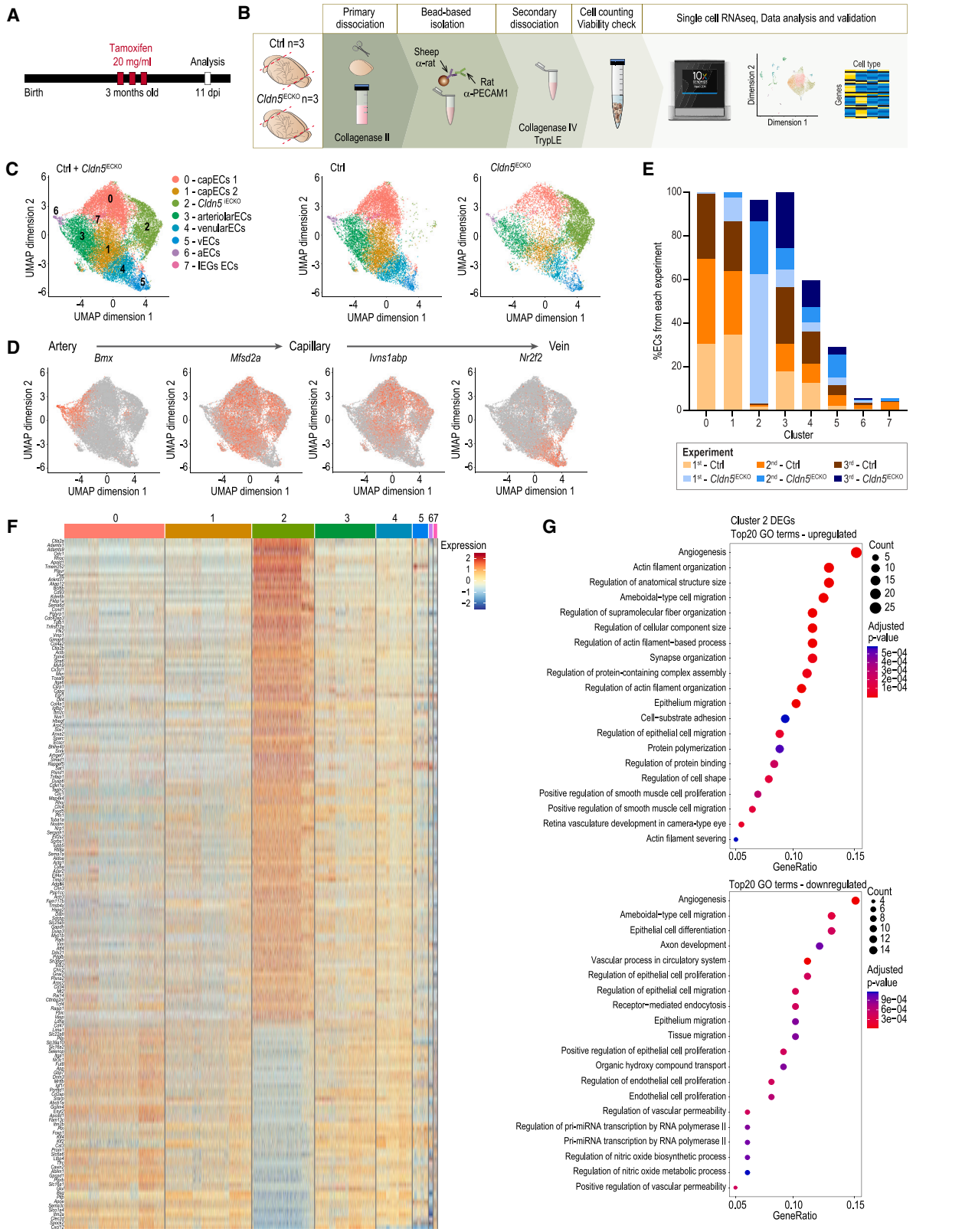

(legend on next page)

PECAM1 in cerebral cortex (approach (2)), which was reduced by ~4% at 3 dpi and by ~19% at 6 dpi (Figure 2E). Together, these time-course experiments show that CLDN5 loss occurs progressively following tamoxifen administration (0–2 dpi) and causes a similarly progressive disruption of the BBB preceding the onset of lethality.

Because leakage of tracers was observed in mice with at least 19% of mosaic Cldn5 loss (Figure 2E), we were keen to investigate whether increased BBB permeability could be detected in constitutive *Cldn5* heterozygous ($^{+/-}$) mice assumed to express 50% less *Cldn5* mRNA. However, we found no detectable leakage of A555Cad in *Cldn5*$^{+/-}$ brains (Figures 2F–2I, and S2E) and similar A555Cad fluorescence in Ctrl and *Cldn5*$^{+/-}$ kidneys (Figures S2E and S2F). Quantitative PCR on cerebral MVFs from *Cldn5*$^{+/-}$ showed ~41% Cldn5 mRNA expression when normalized to *Actb* and 50% when normalized to the endothelium-specific genes *Cdh5* and *Kdr* (Figures 2G and S2G), confirming the expected reduction of *Cldn5* mRNA expression. On the other hand, CLDN5 protein analysis by both western blot on isolated cerebral MVFs (Figures 2H, S2H, S2I, and S2J) and immunostainings (Figure 2I) failed to reveal any significant reduction in CLDN5 protein in *Cldn5*$^{+/-}$ when compared to *Cldn5*$^{+/+}$. We furthermore did not observe any increased lethality in *Cldn5*$^{+/-}$ mice. These observations demonstrate that ablation of both alleles of the *Cldn5* gene is required for sufficient CLDN5 protein loss to cause BBB impairment, neurological symptoms, and death in *Cldn5*^{iECKO} mice. They also demonstrate that complete *Cldn5* gene ablation is deleterious even when it occurs in a minority population of the brain endothelial cells in the mosaic *Cldn5*^{iECKO} mice.

scRNA-seq analysis reveals profound transcriptomic changes in Cldn5^{iECKO} brain endothelial cells

Because immunofluorescence analyses failed to reveal endothelial cell abnormalities other than mosaic loss of CLDN5 and junctional disruption, we performed scRNA-seq to obtain unbiased information about endothelial gene expression in the *Cldn5*^{iECKO} brain vasculature. Vascular cells were isolated from the cerebrums of three *Cldn5*^{iECKO} and three Ctrl mice 11 days after tamoxifen induction and analyzed using the 10x Genomics platform (Figures 3A and 3B). Twelve clusters of a total of 25,186 single-cell transcriptomes that passed quality control were annotated based on cell-specific marker gene expression[3,34] (Figures S3A and S3B; Table S2). As previously reported,[35] a majority of the cells isolated using this approach were endothelial cells. The two other major non-endothelial cell types were mural cells (pericytes and vascular smooth muscle cells) and microglia. The endothelial cells formed two distinct islands in uniform manifold approximation and projection (UMAP), a major island corresponding to *Cldn5-positive/Plvap*-negative BBB endothelium (encompassing clusters 0, 1, 2, 4, 8, 9) and a second minor island corresponding to *Cldn5*-negative/*Plvap*-positive endothelium (cluster 6) (Figures S3A and S3B). In agreement with previous reports on the scRNA-seq profile of fenestrated choroid plexus endothelial cells,[35–37] the minor island, which was equally contributed by Ctrl and *Cldn5*^{iECKO} mice, was positive also for other choroid plexus endothelial markers, including *Esm1*, *Gpihbp1*, and *Cd24a* (Figure S3C). Immunostainings on two 11-dpi litters (Ctrl n = 7, *Cldn5*^{iECKO} n = 8) confirmed that PLVAP-positive endothelium was detected in the choroid plexus, whereas no PLVAP-positive endothelial cells were detected in the brain parenchyma of mosaic *Cldn5*^{iECKO} BBB (Figure S3D). We therefore conclude that the endothelial cells of the minor island derive from choroid plexus and possibly circumventricular organs that are also known to harbor fenestrated endothelial cells, but not from *Cldn5*$^{-}$ BBB endothelial cells in mosaic *Cldn5*^{iECKO} mice.

Subclustering of the 20,911 endothelial cells present in the major BBB endothelial island yielded eight cell clusters (Figure 3C; Table S3). These clusters were largely organized into arterio-venous zonation pattern, as described previously[3] (Figures 3C and 3D). Cells from three independent experiments were represented at roughly similar proportions in most clusters, demonstrating lack of batch effects (Figure 3E). Only the smallest cluster (no. 7), which was composed of lower-quality cells with high counts of immediate-early genes (IEGs), was preferentially derived from one experiment (Figures 3E and S3E–S3G; Table S3 cluster 7). Clusters 0 and 1, annotated as BBB capillary endothelial cells, were mainly contributed by Ctrl mice, whereas cluster 2 was mainly contributed by *Cldn5*^{iECKO} mice (Figures 3C and 3E). This reciprocity, combined with cluster 2 being the nearest neighbor of the capillary clusters 0 and 1 in UMAP, suggest that cluster 2 represents BBB capillary endothelial cells in *Cldn5*^{iECKO} mice (Figures 3C and 3D). In contrast, the arteriolar, venular, venous, and arterial clusters 3, 4, 5, and 6, respectively, contained similar proportions of cells from Ctrl and *Cldn5*^{iECKO} mice, suggesting that the transcriptional change observed in *Cldn5*^{iECKO} mice is limited to the capillaries.

Analyses of differentially expressed genes (DEGs) between the clusters showed that cluster 2 displayed the largest number of DEGs of all endothelial clusters (Figure 3F; Table S3). Gene Ontology (GO) analysis of cluster 2-specifc upregulated DEGs revealed GO terms associated with angiogenesis and actin filament organization (Figure 3G; Table S4). These DEGs (173 in total) included several known markers of angiogenesis, such

Figure 3. scRNA-seq dataset obtained from brain microvascular fragments

(A) Tamoxifen regime for *Cldn5* deletion and analyses.

(B) Schematic overview of the microvascular fragment isolation from the mouse cerebrums (three independent experiments).

(C) Uniform manifold approximation and projection (UMAP) of the 20,911 pure endothelial cells from the dataset clustered into eight clusters (0–7) as well as the separate UMAPs showing only cells from Ctrl mice and cells from *Cldn5*^{iECKO} mice.

(D) UMAPs of arterio-venous marker expressions throughout the endothelial cell clusters. *Bmx*, a marker of arterioles; *Mfsd2a* and *Ivns1abp*, markers of capillaries; and *Nr2f2*, a marker of venules. The choice of arterio-venous markers was based on Vanlandewijck et al.[3] (E) Percentage of endothelial cells from each experiment and genotype in each endothelial cell cluster (0–7).

(F) Heatmap illustrating cluster 2 DEG expression across all endothelial cell clusters. Genes with PCT.1 values >0.5 (Table S3) are depicted on the heatmap.

(G) Gene Ontology (GO) analysis of cluster 2 top 20 up- and downregulated DEGs. See also Figure S3.

as *Apold1*, *Angpt2*, *Mcam*, *Fscn1*, *Dll4*, *Apln*, *Plxnd1*, *Cd93*, *Adm*, and *Kit*,[38,39] as well as markers of basement membrane and extracellular matrix turnover, including *Adamts1*, *Adamts9*, *Col4a1*, *Col4a2*, *Nid1*, *Nid2*, and *Sparc.* We recently identified an endothelial tip cell transcriptome[20]; however, only one of the tip cell markers, *Mcam*, was upregulated in cluster 2. Lack of morphologically discernable tip cells was also apparent from the numerous PECAM1-stained *Cldn5*^{iECKO} brain sections that were analyzed throughout this study. Thus, the upregulated expression of an angiogenesis-related gene program in cluster 2 does not seem to reflect the formation of endothelial tip cells and angiogenic sprouting. Of note, none of the adherens- or tight-junction transcripts were significantly changed in cluster 2 (Figure S3H). Interestingly, among the significantly downregulated DEGs in cluster 2 (79 in total), several BBB-specific transporters (*Slco1a4*, *Slc16a1*, *Tfrc*, *Abcb1a*, and *Slc38a5*) and cytokines, growth factors, their regulators, and targets (*Cxcl12*, *Tgfb2*, *Ptn*, *Ptprb*, *Klf2*, and *Klf4*) were found (Figure 3F; Table S3). These data show that induced brain endothelial *Cldn5* deficiency leads to extensive transcriptional reprogramming of the BBB capillary endothelial cells. We therefore asked whether this response is directly and cell-autonomously coupled to the loss of CLDN5 by the endothelial cells or, alternatively, whether it represents secondary and non-cell-autonomous changes triggered by the BBB leakage and resulting changes in the local brain parenchymal microenvironment.

Distinguishing cell-autonomous from non-cell-autonomous changes in Cldn5^{iECKO} brain endothelium

We initially assumed that cluster 2 corresponded to *Cldn5* mRNA-negative (*Cldn5*$^{-}$) cells, but this assumption turned out to be wrong, as follows. The combination of high *Cldn5* expression in brain endothelial cells[3] and the fact that the entire *Cldn5* gene is flanked by *LoxP* sites in the targeted locus (Figure S1A) made it informative to assess presence (*Cldn5*$^{+}$) or absence (*Cldn5*$^{-}$) of *Cldn5* mRNA sequence reads in single cells. Accordingly, we found that 99.3% of all Ctrl single-cell endothelial transcriptomes were *Cldn5*$^{+}$. We speculate that the 0.7% *Cldn5*$^{-}$ (Figure 4A) cells among the Ctrl BBB endothelial cells represent rare stochastic technical dropouts since CLDN5 protein is uniformly expressed in BBB vasculature in Ctrl brains, supposedly reflecting 100% *Cldn5*$^{+}$ cells (Figures 1C and S1D). In contrast, *Cldn5*^{iECKO} mice showed 84.6% *Cldn5*$^{+}$ and 15.4% *Cldn5*$^{-}$ single-cell transcriptomes. Although 15.4% was lower than expected from the average *Cldn5* KO efficiency assessed by qPCR (~35%), it fell within the observed range of variability observed in all approaches used to study the degree of Cldn5 mosaicism (approaches 1–3, see above) (Figure 1F). To visualize the raw data from this analysis, single cells were depicted as color-coded bars according to the genotype (Ctrl or *Cldn5*^{iECKO}) and presence or absence of the *Cldn5* mRNA counts (*Cldn5*$^{+}$ or *Cldn5*$^{-}$): blue = *Cldn5*$^{+}$ in Ctrl; dark blue = *Cldn5*$^{-}$ in Ctrl; orange = *Cldn5*$^{+}$ in *Cldn5*^{iECKO}; red = *Cldn5*$^{-}$ in *Cldn5*^{iECKO} (Figure 4B). The gene expression patterns of all genes across the endothelial cell clusters are available gene by gene as bar plot data at https://sicof.medh.ki.se/cldn5/EC.

Cldn5^{-} cells from *Cldn5*^{iECKO} were enriched in cluster 2 but present in all clusters, including arteries, arterioles, venules, and veins (Figures 4A, 4B, and S4A). The presence of CLDN5 protein-negative cells in arterioles and venules was confirmed on tissue sections (Figure S4B). Surprisingly, the majority of cells (2,978 cells) in the *Cldn5*^{iECKO}-dominated cluster 2 were *Cldn5*$^{+}$ and only about 15% of them (555 cells) *Cldn5*$^{-}$ (Figures 4A, 4B, and S4A). These results show that lack of *Cldn5* mRNA by the individual cells had little impact on their dispersal to cluster 2, which instead depended on the microenvironment associated with brain capillaries in *Cldn5*^{iECKO} mice.

Intra-cluster comparison between *Cldn5*$^{-}$ (red) and *Cldn5*$^{+}$ cells (orange) from *Cldn5*^{iECKO} mice showed negligible differences beyond *Cldn5* (Table S5). A possible exception was *Cx3cl1*, which showed higher counts in *Cldn5*$^{-}$ cells compared to *Cldn5*$^{+}$ cells in clusters 0, 2, and 3 (Figure 4B). Within venous cluster 5, a small but statistically significant downregulation of clathrin interactor 1 (*Clint1*) was also revealed in *Cldn5*^{iECKO} *Cldn5*$^{-}$ cells (Figure 4B).

To further explore possible (lack of) cell-autonomous transcriptional consequences of Cldn5 loss, we analyzed cultured bEnd.3 brain endothelial cells by RNA sequencing following treatment with *Cldn5*-targeting small interfering RNA (siRNA) (si*Cldn5*) or non-targeting control siRNA (siCtrl) at different concentrations and different treatment durations (Figure S4C). Comparison of all tested conditions revealed that the samples treated with si*Cldn5* showed minor changes compared to siCtrl (Figures S4D–S4F). Moreover, none of the few DEGs (Figures S4G and S4H) between si*Cldn5* and siCtrl-treated cells (Table S6) were significantly different in *Cldn5*$^{-}$ cells *in vivo* in mosaic *Cldn5*^{iECKO} mice (Figure S4I). In conclusion, both *in vivo* and *in vitro* data suggest that loss of *Cldn5* in brain endothelial cells does not have direct (cell-autonomous) transcriptional changes in endothelial cells beyond *Cldn5* itself and, therefore, that the transcriptional activation/reaction seen in cluster 2 reflects an indirect (i.e., non-cell-autonomous) response of the endothelium to BBB leakage and ensuing changes in the local microenvironment, possibly involving other cell types than the endothelial cells.

The non-cell-autonomous effects of mosaic Cldn5 KO were further illustrated by immunofluorescent staining of SLC16A1 in brain tissue at 11 dpi (Figure 4C). Two litters with ~35% EYFP expression were used for this analysis (Figure 4D). Overall, SLC16A1 staining was weaker in *Cldn5*^{iECKO} brain in agreement with *Slc16a1* mRNA reduction in cluster 2 (Figures 4B; Table S3), but it did not correlate with *Cldn5* loss at the cellular level. Instead, average SLC16A1 longitudinal capillary expression was comparable between *Cldn5*^{iECKO} and Ctrl (Figure 4E) and ~61% of the EYFP^{+} capillaries were SLC16A1^{+} in the *Cldn5*^{iECKO} cortex (Figure 4F). No correlation ($r = -0.1617$) was found between the percentages of SLC16A1 longitudinal expression and EYFP recombination in the capillaries of *Cldn5*^{iECKO} mouse cortex (Figure 4G). Thus, the reduced expression of SLC16A1 is an example of a non-cell-autonomous change of *Cldn5*^{iECKO} brain endothelium *in vivo*.

Increased inflammation in the adult Cldn5^{iECKO} mouse brain

Since scRNA-seq revealed increased expression of *Cx3cl1*, which encodes a ligand for the immune-cell receptor CX3CR1,[40] in the endothelial cell cluster 2 in *Cldn5*^{iECKO} brains (average log 2 fold

CellPress
OPEN ACCESS

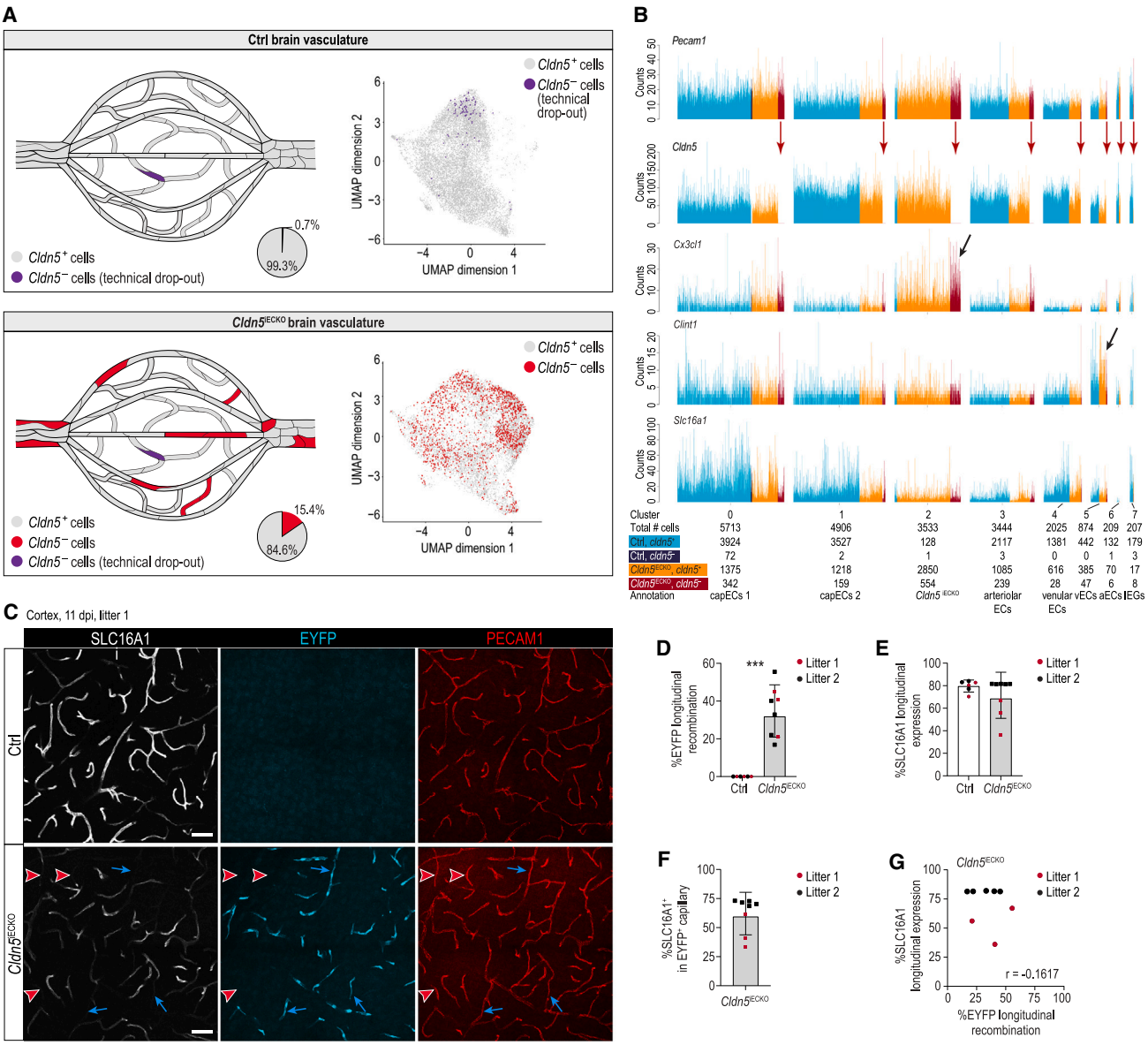

Figure 4. Characterization of transcriptional changes in the endothelium of adult *Cldn5*^{iECKO}

(A) Schematic representation of *Cldn5*$^{+}$ and *Cldn5*$^{-}$ cells in Ctrl and *Cldn5*^{iECKO} mice. Pie charts illustrate the percentage of *Cldn5*$^{+}$ and *Cldn5*$^{-}$ cells in each genotype. UMAPs illustrate the *Cldn5*$^{-}$ cell distribution throughout the endothelial cell clusters.

(B) Bar plots showing *Pecam1*, *Cldn5*, *Cx3cl1*, *Clint1*, and *Slc16a1* counts in the endothelial cell clusters 0–7. Red arrows point to *Cldn5*$^{-}$ cells. Black arrow in *Cx3cl1* bar plot marks *Cx3cl1* upregulation in *Cldn5*$^{-}$ cells in cluster 2. Black arrow in *Clint1* bar plot marks *Clint1* downregulation in *Cldn5*$^{-}$ cells in cluster 5.

(C) Representative images from the cortex of *Cldn5*^{iECKO} and Ctrl of litter 1 analyzed at 11 dpi (n = 3). PECAM1^{+}EYFP^{+} vascular stretches with loss of SLC16A1 staining are marked with blue arrows. PECAM1^{+}EYFP^{-} vascular stretches with loss of SLC16A1 staining are marked with red arrowheads. Scale bars, 25 μm.

(D) Quantification of %EYFP longitudinal recombination relative to PECAM1 in the mouse cortex of *Cldn5*^{iECKO} and Ctrl. Two litters, Ctrl n = 6, *Cldn5*^{iECKO} n = 8.

(E) Quantification of %SLC16A1 longitudinal capillary expression relative to PECAM1 in the mouse cortex of *Cldn5*^{iECKO} and Ctrl. Two litters, Ctrl n = 6, *Cldn5*^{iECKO} n = 8.

(F) Quantification of %EYFP^{+} capillaries with SLC16A1^{+} longitudinal capillary expression in the cortex of *Cldn5*^{iECKO} mice (n = 8).

(G) Dot plot of the correlation of %SLC16A1 longitudinal expression with %EYFP longitudinal recombination in the cortex of *Cldn5*^{iECKO} and Ctrl. Pearson correlation coefficient (r) = −0.1617. (D) The data were not normally distributed so nonparametric Mann-Whitney U test was used to evaluate significance. (E) The significance of normally distributed data was evaluated using unpaired two-tailed t test with Welch's correction. Data are presented as geometric mean with geometric SD. (D) ***p < 0.001. See also Figure S4.

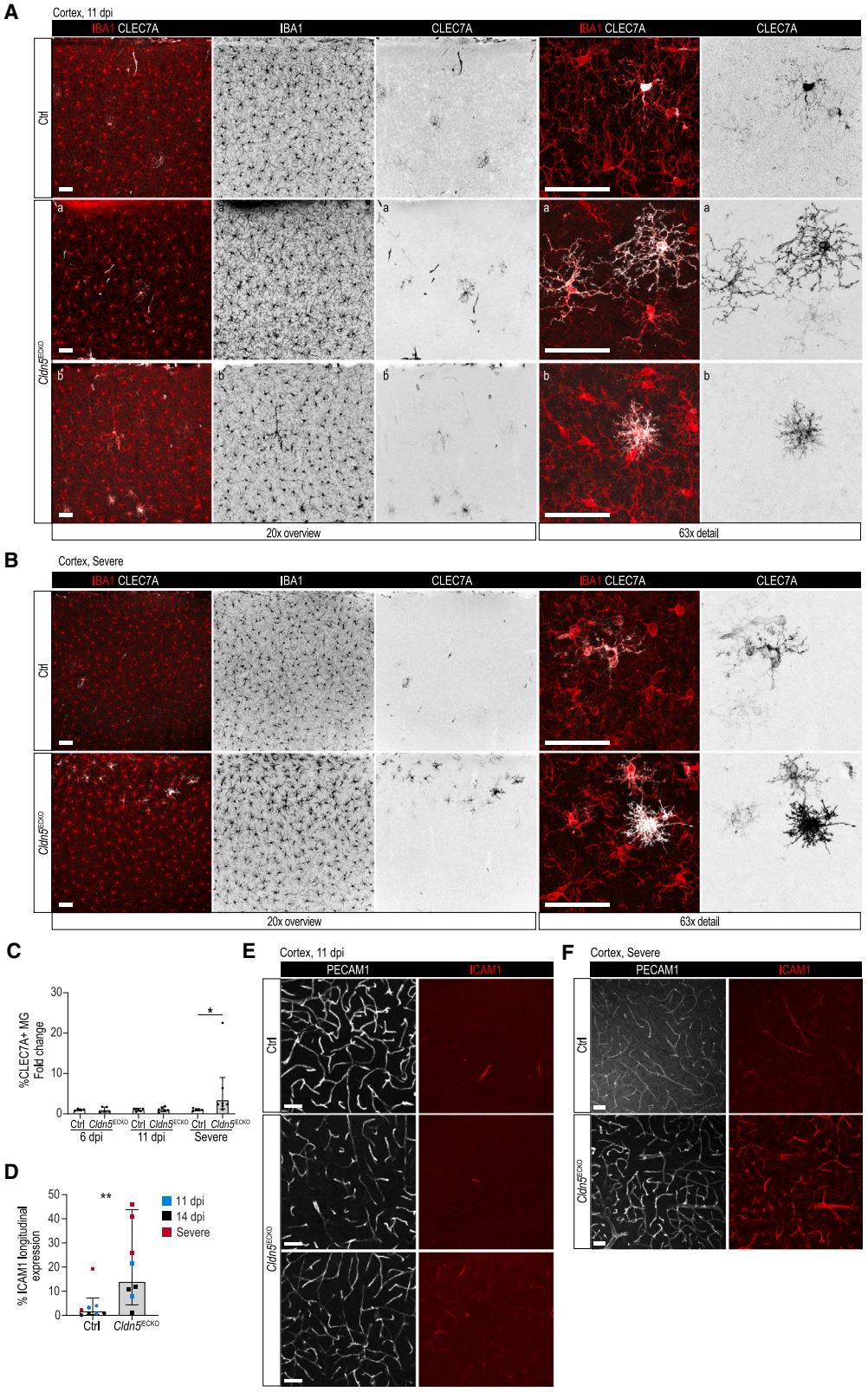

(legend on next page)

change (avg_log2FC) = 1.08; Figure 4B; Table S3 cluster 2), we investigated glial and endothelial responses in the *Cldn5*^{iECKO} brain sections. IBA1 immunostainings revealed no apparent change in microglia morphology at 6 dpi in cerebral cortex and 11 dpi in cerebral cortex, thalamus, and hippocampus, the time points when the vascular leakage was already significant (Figures 5A and S5A–S5C). However, there was clear microglial reactivity in the *Cldn5*^{iECKO} brain cerebral cortex, thalamus, and hippocampus in the two litters displaying the most severe symptoms (Figures 5B, S5B, and S5C). While IBA1^{+} cells in Ctrl brains extended characteristic long, thin, and ramified processes (Figures 5A, 5B, and S5A–S5C), the IBA1^{+} cells found around the capillaries in severe *Cldn5*^{iECKO} brains were enlarged and displayed shorter and thicker processes (Figures 5B, S5B, and S5C). Quantification of IBA1^{+} cells revealed no changes in microglia numbers between *Cldn5*^{iECKO} and Ctrl at any time points and regions analyzed (Figures S5D–S5F). Gene signatures of reactive microglia have been extensively characterized during recent years (reviewed in Butovsky and Weiner[41]). Immunostainings with one of the reported reactive microglia markers, C-type lectin domain-containing 7A (CLEC7A), revealed increased number of CLEC7A^{+}/IBA1^{+} microglia with a clear reactive morphology and high CLEC7A expression in the two severe litters (Figures 5B, 5C, S5B, S5C, S5G, and S5H). Some CLEC7A^{high} microglia were also observed in an 11-dpi-litter cerebral cortex (Figure 5A) and lower levels of CLEC7A was detectable in some microglia in *Cldn5*^{iECKO} brains at 6 and 11 dpi, although this level of expression was seen also in Ctrl brain microglia that displayed normal morphology (Figures 5A, 5B, 5C, S5A–S5C, S5G, and S5H). Cells with perivascular location were detected in cerebral cortex of all analyzed brains, presumably representing perivascular macrophages (Figures 5A, 5B, and S5A–S5C).

In addition, glial fibrillary acidic protein (GFAP), a marker of astrocyte reactivity, was seen throughout the cortex of *Cldn5*^{iECKO} severely affected brains, whereas astrocytes in the cortex of Ctrl mice were GFAP positive only around bigger vessels (Figure S5I). Moreover, extravasated CD45^{+} leukocytes were observed in the brain parenchyma of the severe *Cldn5*^{iECKO} mice but not at earlier time points (Figure S5J).

The glial reactivity, immune-cell extravasation, and the fact that angiogenesis was the top GO term in *Cldn5*^{iECKO}-dominating cluster 2 prompted us to further assess endothelial activation/inflammation at different time points (11, 14, and severe) using known markers. At 11 dpi, scRNA-seq did not reveal any differences in ICAM1 expression between *Cldn5*^{iECKO} and Ctrl brains (Figure S5K). ICAM1 immunofluorescent staining of brain sections at 11 dpi showed variable expression (Figures 5D and 5E), which, however, became more pronounced and widespread in the severe litter (Figures 5D and F). Although *Angpt2* was upregulated in cluster 2 (avg_log2FC = 1.3260; Table S3 cluster 2), ANGPT2 immunofluorescence was negative at 11 dpi (Ctrl n = 6, *Cldn5*^{iECKO} n = 5) but massively upregulated in *Cldn5*^{iECKO} capillaries in the most severely affected mice (Figure S5L). Collectively, these results suggest that inflammatory responses in both endothelial and glial cells contribute to the non-cell-autonomous changes of the Cldn5-deficient brain endothelium.

DISCUSSION

Here, we investigated the consequences of adult-induced mosaic *Cldn5* loss in the mouse brain. Within a few days after induction of *Cldn5* gene deletion, we observed CLDN5 protein loss, increased BBB leakage, and widespread non-cell-autonomous changes in both endothelial and glial cells. The rapidly onsetting neuroinflammatory condition culminated in seizures and ensuing lethality from 10 dpi. These results demonstrate the critical importance of CLDN5 in the adult BBB and the pathogenic consequences of CLDN5 dysregulation, raising caution about CLDN5 targeting as a safe approach to improve drug delivery to the brain.

Our model allowed us to study size selectivity of tight junctions for paracellular molecular passage across the BBB. Previous work on constitutive *Cldn5* KOs reported leakage of tracers up to 742 Da in size across the BBB while passage of larger molecules remained restricted.[16] In contrast, the BBB of adult-inducible mosaic *Cldn5*^{iECKO} mice was permeable for tracers up to 10 kDa in size in agreement with findings in *cldn5a*−/− zebrafish model.[17] The difference in size restriction between the two mouse models may have technical or biological reasons. Technical differences include tracer circulation times and detection. While we let the tracers circulate for 2–16 h (depending on the tracer size; see Table S1) Nitta et al.[16] let tracers circulate for 5 min. Also, Nitta et al.[16] measured tracer extravasation by fluorescence microscopy and we used a sensitive fluorescence plate reader. Among biological explanations, it is possible that inflammatory responses to primary BBB disruption may differ in constitutive *Cldn5* KO neonates (Nitta et al.[16]) and adult-inducible mosaic *Cldn5*^{iECKO} mice. Specifically, the non-cell-autonomous inflammatory changes in both glial and endothelial cells in *Cldn5*^{iECKO} mice may trigger additional modes of BBB leakage beyond what is cell-autonomously caused by disruption of endothelial tight junctions. Conversely, it is possible that constitutive *Cldn5* KO may trigger compensatory mechanisms during embryonic development that limit or partially rescue BBB leakage

Figure 5. Characterization of microglial phenotypes and ICAM1 expression in adult *Cldn5*^{iECKO} and Ctrl brains

(A and B) Representative images of CLEC7A and IBA1 microglia from the cortex of *Cldn5*^{iECKO} ([a] field 1, [b] field 2) and Ctrl. Scale bars, 50 μm. (A) At 11 dpi, two litters, n = 6; (B) severe, two litters, Ctrl n = 5, *Cldn5*^{iECKO} n = 7.

(C) Quantification of %CLEC7A^{+}/IBA1^{+} cells per field in the cerebral cortex.

(D) Quantification of %ICAM1 longitudinal capillary expression normalized to PECAM1 longitudinal expression in the capillary bed of the brain cortex. Three litters analyzed 11 dpi (blue), 14 dpi (black), and severe (red), n = 8.

(E and F) Representative images from the cortex of *Cldn5*^{iECKO} and Ctrl. (E) Ctrl n = 3, *Cldn5*^{iECKO} n = 2; (F) Ctrl n = 2, *Cldn5*^{iECKO} n = 3. Scale bars, 25 μm. (C) At 6 dpi, the data were normally distributed and therefore the significance of the data was evaluated using unpaired two-tailed t test with Welch's correction. In (C) (11 dpi and severe) and (D) (for the pooled dpi values), the data were not normally distributed so nonparametric Mann-Whitney U test was used to evaluate significance. Data are presented as geometric mean with geometric SD. *p < 0.05, **p = 0.01. See also Figure S5.

primarily caused by CLDN5 loss.[16] While *in vivo* models clearly have limitations regarding their ability to directly assess the size selectivity of tight junctions at the BBB, information about BBB breakdown as a progressive event starting with tight junction impairment may be more relevant from a pathophysiological perspective. Interestingly, it also opens the possibility to assess whether/how non-cell-autonomous inflammatory responses in endothelial cells and glial cells contribute to size selectivity and other characteristics of the BBB.

The non-cell-autonomous transcriptomic changes in *Cldn5*^{iECKO} brain capillary endothelial cells are likely secondary to BBB disruption, leading either to responses directly in the endothelial cells or triggering responses in other brain parenchymal cells (microglia and astrocytes), which, in turn, affect the endothelium. The latter scenario seems plausible based on several observations, including the astrocytic and microglial reaction, the presence of CD45^{+} leukocytes in the brain parenchyma, and the increased expression of endothelial ICAM1 in *Cldn5*^{iECKO} brain capillaries. BBB disruption has been observed in neurodegenerative diseases such as MS,[42] Alzheimer's,[43] and Parkinson's disease,[44] which showed glial inflammation at variable times during the course of the diseases. The extravasation of blood-borne molecules and toxins into the brain parenchyma has indeed been proposed to induce rapid reactions in microglia and astrocytes,[45–48] which in turn could aggravate the BBB disruption via secretion of growth factors such as vascular endothelial growth factor A (VEGFA).[49] Reactive glial cells could also cause neuronal damage and hyperexcitability via various cytokines.[50–52] Microglial reaction and neurodegeneration could also be caused by the infiltration of leukocytes when the BBB is disrupted.[53] It is still unclear from these correlations if an early disruption of the BBB observed in brain diseases is causal to any aspect of the disease pathogenesis or whether it is a consequence without pathogenic relevance. However, our present study illustrates how primary BBB opening and ensuing reciprocal inflammatory engagement of multiple cell types in the brain parenchyma may have deleterious consequences for brain function. Specifically, our results suggest that primary BBB leakage causes rapid induction of glial responses, and that these or other resulting microenvironmental changes trigger further responses in the endothelial cells, possibly even with further negative effects on BBB function.

We found the Angpt2 upregulation in the endothelium of *Cldn5*^{iECKO} brains interesting. ANGPT2 has been described as an antagonist of the TIE2 receptor that disrupts the vasculature and promotes inflammation.[54–56] However, the effect of ANGPT2 on the vasculature is not yet completely understood, as it can have context-dependent agonistic activity, e.g., in the absence of vascular endothelial protein tyrosine phosphatase (VE-PTP) in the lymphatic vasculature.[57,58] ANGPT2 was found to protect the BBB in *Pdgfb*$^{ret/ret}$ mice, a pericyte-deficient mouse model with developmental pericyte loss.[20] Furthermore, *Angpt2*$^{-/-}$ mice display increased BBB permeability of fluorescent tracers and show a disrupted CLDN5 expression pattern.[20] The importance of the upregulation of Angpt2 in *Cldn5*^{iECKO} mice will remain a topic for further study.

Cldn5 has been attempted as a target to increase drug delivery into the brain.[59–62] However, the risks associated with the opening of paracellular junctions at the BBB have not been extensively analyzed. We found first signs of 1-kDa A555Cad leakage already at ~6 days after induction *of Cldn5* gene deletion, which may reflect the dynamics of tamoxifen-induced gene deletion as well as of CLDN5 protein decay. We also found that molecules up to 10 kDa in molecular weight (MW) passed into the brain. However, regardless of BBB size selectivity in the *Cldn5* deficient state, it remains to be determined how drugs of different physiochemical properties may pass through disrupted paracellular tight junctions in brain endothelial cells. Previous work with *Pdgfb*$^{ret/ret}$ mice showed that small lipophilic pharmaceuticals that are substrates for efflux transporters such as P-glycoprotein are blocked from passing the BBB under circumstances when passage of large hydrophilic molecules occurs.[63] In *Pdgfb*$^{ret/ret}$ mice, the BBB leakage occurs both via disruption of paracellular junctions and increased transcytosis. Whether small lipophilic drugs are similarly blocked from entering through disrupted tight junctions remains to be investigated. Regardless of such considerations, our results raise caution concerning CLDN5 targeting for enhanced drug delivery to the brain. More analyses are needed to assess whether safe levels of CLDN5 downregulation exist that provide a sufficient time window for meaningful drug delivery across the BBB.

Limitations of the study

A major limitation in the interpretation of the time courses and sequences of events in these experiments is that tracer quantification and glial reactivity/endothelial inflammation had to be analyzed in separate animals and litters for technical reasons. The variability in the observed recombination efficiencies and phenotypes, even within the same litter, complicates conclusions about the exact time course and progression of events.

STAR★METHODS

Detailed methods are provided in the online version of this paper and include the following:

- KEY RESOURCES TABLE
- RESOURCE AVAILABILITY
  - Lead contact
  - Materials availability
  - Data and code availability
- EXPERIMENTAL MODEL AND STUDY PARTICIPANT DETAILS
  - Experimental mice
- METHOD DETAILS
  - Microvascular fragment isolation for quantitative PCR (qPCR), western blot and scRNAseq
  - qPCR
  - Western blot
  - BBB permeability
  - Immunofluorescence stainings
  - EYFP longitudinal recombination and CLDN5 longitudinal expression analysis in cerebral cortex
  - Endothelial cell quantification in cerebral cortex
  - EYFP longitudinal recombination and CLDN5 longitudinal expression analysis in cerebral cortex, hippocampus and thalamus – Comparative experiment

- MVF isolation and single-cell RNA sequencing using 10x genomics technology
- Bioinformatical analyses of single-cell RNA sequencing
- Gene Ontology analyses
- SLC16A1 longitudinal expression quantification and EYFP correlation in cerebral cortex
- Cldn5 downregulation in bEnd.3 cell culture and RNA-seq
- ICAM1 longitudinal expression analysis in cerebral cortex
- IBA1+ and CLEC7A + cell number quantification in cerebral cortex, thalamus and hippocampus

● QUANTIFICATION AND STATISTICAL ANALYSIS

SUPPLEMENTAL INFORMATION

Supplemental information can be found online at https://doi.org/10.1016/j.celrep.2024.113911.

ACKNOWLEDGMENTS

We thank C. Olsson, H. Leksell, P. Peterson, and J. Chmielniakova for technical help and the Single Cell Core Facility at Flemingsberg Campus (SICOF), Karolinska Institute, for their single-cell sequencing services. This study was supported by the Swedish Research Council (M.A.M., 2023-02655; C.B., 2015–00550; K.G., 2021-04896), the European Research Council (C.B., AdG294556), the Leducq Foundation (C.B., 14CVD02 and 22CVD01; M.A.M. and C.B., 23CVD02), Swedish Cancer Society (C.B., 150735), Knut and Alice Wallenberg Foundation (C.B., 2015.0030; C.B. and K.G., 2020.0057), the Innovative Medicines Initiative (C.B., IM2PACT-807015), and Innovative ways to fight Alzheimer's disease- Leif Lundblad Family and others (M.V.). The Campbell lab is supported by grants from Science Foundation Ireland (SFI) (Eye-D-21/SPP/3732), Enterprise Ireland, The Irish Research Council (IRC), and by a research grant from SFI under grant number 16/RC/3948 and co funded under the European Regional Development fund by FutureNeuro industry partners. The Campbell lab is also supported by a European Research Council (ERC) grant, Retina Rhythm (864522).

AUTHOR CONTRIBUTIONS

Conceptualization, M.A.M. and C.B.; methodology, M.A.M., B.L., and C.B.; investigation, E.V.-L., M.A.M., W.L., B.L., A.R., N.H., Z.E., C.O., I.N., and M.V.; data curation, G.M.; writing – original draft, E.V.-L. and M.A.M.; writing – review & editing, E.V.-L., M.A.M., and C.B.; visualization, E.V.-L. and M.A.M.; funding acquisition, M.A.M., M.C., K.G., M.V., and C.B.; supervision, M.A.M. and M.C.

DECLARATION OF INTERESTS

The authors declare no competing interests.

Received: July 14, 2023
Revised: December 19, 2023
Accepted: February 16, 2024
Published: March 5, 2024

REFERENCES

1. Begley, D.J. (2004). ABC transporters and the blood-brain barrier. Curr. Pharm. Des. *10*, 1295–1312. https://doi.org/10.2174/1381612043384844.
2. Lin, L., Yee, S.W., Kim, R.B., and Giacomini, K.M. (2015). SLC transporters as therapeutic targets: emerging opportunities. Nat. Rev. Drug Discov. *14*, 543–560. https://doi.org/10.1038/nrd4626.
3. Vanlandewijck, M., He, L., Mäe, M.A., Andrae, J., Ando, K., Del Gaudio, F., Nahar, K., Lebouvier, T., Laviña, B., Gouveia, L., et al. (2018). A molecular atlas of cell types and zonation in the brain vasculature. Nature *554*, 475–480. https://doi.org/10.1038/nature25739.
4. Greene, C., Hanley, N., and Campbell, M. (2019). Claudin-5: gatekeeper of neurological function. Fluids Barriers CNS *16*, 3. https://doi.org/10.1186/s12987-019-0123-z.
5. Krause, G., Winkler, L., Mueller, S.L., Haseloff, R.F., Piontek, J., and Blasig, I.E. (2008). Structure and function of claudins. Biochim. Biophys. Acta *1778*, 631–645. https://doi.org/10.1016/j.bbamem.2007.10.018.
6. Blasig, I.E., Winkler, L., Lassowski, B., Mueller, S.L., Zuleger, N., Krause, E., Krause, G., Gast, K., Kolbe, M., and Piontek, J. (2006). On the self-association potential of transmembrane tight junction proteins. Cell. Mol. Life Sci. *63*, 505–514. https://doi.org/10.1007/s00018-005-5472-x.
7. Rossa, J., Ploeger, C., Vorreiter, F., Saleh, T., Protze, J., Günzel, D., Wolburg, H., Krause, G., and Piontek, J. (2014). Claudin-3 and claudin-5 protein folding and assembly into the tight junction are controlled by non-conserved residues in the transmembrane 3 (TM3) and extracellular loop 2 (ECL2) segments. J. Biol. Chem. *289*, 7641–7653. https://doi.org/10.1074/jbc.M113.531012.
8. Piontek, J., Winkler, L., Wolburg, H., Müller, S.L., Zuleger, N., Piehl, C., Wiesner, B., Krause, G., and Blasig, I.E. (2008). Formation of tight junction: determinants of homophilic interaction between classic claudins. FASEB J *22*, 146–158. https://doi.org/10.1096/fj.07-8319com.
9. Gehne, N., Lamik, A., Lehmann, M., Haseloff, R.F., Andjelkovic, A.V., and Blasig, I.E. (2017). Cross-over endocytosis of claudins is mediated by interactions via their extracellular loops. PLoS One *12*, e0182106. https://doi.org/10.1371/journal.pone.0182106.
10. Wen, H., Watry, D.D., Marcondes, M.C.G., and Fox, H.S. (2004). Selective decrease in paracellular conductance of tight junctions: role of the first extracellular domain of claudin-5. Mol. Cell Biol. *24*, 8408–8417. https://doi.org/10.1128/MCB.24.19.8408-8417.2004.
11. Ishizaki, T., Chiba, H., Kojima, T., Fujibe, M., Soma, T., Miyajima, H., Nagasawa, K., Wada, I., and Sawada, N. (2003). Cyclic AMP induces phosphorylation of claudin-5 immunoprecipitates and expression of claudin-5 gene in blood-brain-barrier endothelial cells via protein kinase A-dependent and -independent pathways. Exp. Cell Res. *290*, 275–288. https://doi.org/10.1016/s0014-4827(03)00354-9.
12. Shen, W., Li, S., Chung, S.H., Zhu, L., Stayt, J., Su, T., Couraud, P.O., Romero, I.A., Weksler, B., and Gillies, M.C. (2011). Tyrosine phosphorylation of VE-cadherin and claudin-5 is associated with TGF-beta1-induced permeability of centrally derived vascular endothelium. Eur. J. Cell Biol. *90*, 323–332. https://doi.org/10.1016/j.ejcb.2010.10.013.
13. Yamamoto, M., Ramirez, S.H., Sato, S., Kiyota, T., Cerny, R.L., Kaibuchi, K., Persidsky, Y., and Ikezu, T. (2008). Phosphorylation of claudin-5 and occludin by rho kinase in brain endothelial cells. Am. J. Pathol. *172*, 521–533. https://doi.org/10.2353/ajpath.2008.070076.
14. Itoh, M., Furuse, M., Morita, K., Kubota, K., Saitou, M., and Tsukita, S. (1999). Direct binding of three tight junction-associated MAGUKs, ZO-1, ZO-2, and ZO-3, with the COOH termini of claudins. J. Cell Biol. *147*, 1351–1363. https://doi.org/10.1083/jcb.147.6.1351.
15. Liebner, S., Kniesel, U., Kalbacher, H., and Wolburg, H. (2000). Correlation of tight junction morphology with the expression of tight junction proteins in blood-brain barrier endothelial cells. Eur. J. Cell Biol. *79*, 707–717. https://doi.org/10.1078/0171-9335-00101.
16. Nitta, T., Hata, M., Gotoh, S., Seo, Y., Sasaki, H., Hashimoto, N., Furuse, M., and Tsukita, S. (2003). Size-selective loosening of the blood-brain barrier in claudin-5-deficient mice. J. Cell Biol. *161*, 653–660. https://doi.org/10.1083/jcb.200302070.
17. Li, Y., Wang, C., Zhang, L., Chen, B., Mo, Y., and Zhang, J. (2022). Claudin-5a is essential for the functional formation of both zebrafish blood-brain barrier and blood-cerebrospinal fluid barrier. Fluids Barriers CNS *19*, 40. https://doi.org/10.1186/s12987-022-00337-9.

18. Knowland, D., Arac, A., Sekiguchi, K.J., Hsu, M., Lutz, S.E., Perrino, J., Steinberg, G.K., Barres, B.A., Nimmerjahn, A., and Agalliu, D. (2014). Stepwise recruitment of transcellular and paracellular pathways underlies blood-brain barrier breakdown in stroke. Neuron *82*, 603–617. https://doi.org/10.1016/j.neuron.2014.03.003.

19. Boyé, K., Geraldo, L.H., Furtado, J., Pibouin-Fragner, L., Poulet, M., Kim, D., Nelson, B., Xu, Y., Jacob, L., Maissa, N., et al. (2022). Endothelial Unc5B controls blood-brain barrier integrity. Nat. Commun. *13*, 1169. https://doi.org/10.1038/s41467-022-28785-9.

20. Mäe, M.A., He, L., Nordling, S., Vazquez-Liebanas, E., Nahar, K., Jung, B., Li, X., Tan, B.C., Chin Foo, J., Cazenave-Gassiot, A., et al. (2021). Single-Cell Analysis of Blood-Brain Barrier Response to Pericyte Loss. Circ. Res. *128*, e46–e62. https://doi.org/10.1161/CIRCRESAHA.120.317473.

21. Alvarez, J.I., Cayrol, R., and Prat, A. (2011). Disruption of central nervous system barriers in multiple sclerosis. Biochim. Biophys. Acta *1812*, 252–264. https://doi.org/10.1016/j.bbadis.2010.06.017.

22. Greene, C., Hanley, N., Reschke, C.R., Reddy, A., Mäe, M.A., Connolly, R., Behan, C., O'Keeffe, E., Bolger, I., Hudson, N., et al. (2022). Microvascular stabilization via blood-brain barrier regulation prevents seizure activity. Nat. Commun. *13*, 2003. https://doi.org/10.1038/s41467-022-29657-y.

23. Wu, N., Zhang, X., Jin, S., Liu, S., Ju, G., Wang, Z., Liu, L., Ye, L., and Wei, J. (2010). A weak association of the CLDN5 locus with schizophrenia in Chinese case-control samples. Psychiatry Res. *178*, 223. https://doi.org/10.1016/j.psychres.2009.11.019.

24. Greene, C., Hanley, N., and Campbell, M. (2020). Blood-brain barrier associated tight junction disruption is a hallmark feature of major psychiatric disorders. Transl. Psychiatry *10*, 373. https://doi.org/10.1038/s41398-020-01054-3.

25. Menard, C., Pfau, M.L., Hodes, G.E., Kana, V., Wang, V.X., Bouchard, S., Takahashi, A., Flanigan, M.E., Aleyasin, H., LeClair, K.B., et al. (2017). Social stress induces neurovascular pathology promoting depression. Nat. Neurosci. *20*, 1752–1760. https://doi.org/10.1038/s41593-017-0010-3.

26. Wakayama, E., Kuzu, T., Tachibana, K., Hirayama, R., Okada, Y., and Kondoh, M. (2022). Modifying the blood-brain barrier by targeting claudin-5: Safety and risks. Ann. N. Y. Acad. Sci. *1514*, 62–69. https://doi.org/10.1111/nyas.14787.

27. Pitulescu, M.E., Schmidt, I., Benedito, R., and Adams, R.H. (2010). Inducible gene targeting in the neonatal vasculature and analysis of retinal angiogenesis in mice. Nat. Protoc. *5*, 1518–1534. https://doi.org/10.1038/nprot.2010.113.

28. Srinivas, S., Watanabe, T., Lin, C.S., William, C.M., Tanabe, Y., Jessell, T.M., and Costantini, F. (2001). Cre reporter strains produced by targeted insertion of EYFP and ECFP into the ROSA26 locus. BMC Dev. Biol. *1*, 4. https://doi.org/10.1186/1471-213x-1-4.

29. Álvarez-Aznar, A., Martínez-Corral, I., Daubel, N., Betsholtz, C., Mäkinen, T., and Gaengel, K. (2020). Tamoxifen-independent recombination of reporter genes limits lineage tracing and mosaic analysis using CreER(T2) lines. Transgenic Res. *29*, 53–68. https://doi.org/10.1007/s11248-019-00177-8.

30. Sundaram, M.V., and Cohen, J.D. (2017). Time to make the doughnuts: Building and shaping seamless tubes. Semin. Cell Dev. Biol. *67*, 123–131. https://doi.org/10.1016/j.semcdb.2016.05.006.

31. Kotini, M.P., Mäe, M.A., Belting, H.G., Betsholtz, C., and Affolter, M. (2019). Sprouting and anastomosis in the Drosophila trachea and the vertebrate vasculature: Similarities and differences in cell behaviour. Vascul. Pharmacol. *112*, 8–16. https://doi.org/10.1016/j.vph.2018.11.002.

32. Campbell, M., Kiang, A.S., Kenna, P.F., Kerskens, C., Blau, C., O'Dwyer, L., Tivnan, A., Kelly, J.A., Brankin, B., Farrar, G.J., and Humphries, P. (2008). RNAi-mediated reversible opening of the blood-brain barrier. J. Gene Med. *10*, 930–947. https://doi.org/10.1002/jgm.1211.

33. Armulik, A., Genové, G., Mäe, M., Nisancioglu, M.H., Wallgard, E., Niaudet, C., He, L., Norlin, J., Lindblom, P., Strittmatter, K., et al. (2010). Pericytes regulate the blood-brain barrier. Nature *468*, 557–561. https://doi.org/10.1038/nature09522.

34. Zeisel, A., Hochgerner, H., Lönnerberg, P., Johnsson, A., Memic, F., van der Zwan, J., Häring, M., Braun, E., Borm, L.E., La Manno, G., et al. (2018). Molecular Architecture of the Mouse Nervous System. Cell *174*, 999–1014.e22. https://doi.org/10.1016/j.cell.2018.06.021.

35. Bjørnholm, K.D., Del Gaudio, F., Li, H., Li, W., Vazquez-Liebanas, E., Mäe, M.A., Lendahl, U., Betsholtz, C., Nilsson, P., Karlström, H., and Vanlandewijck, M. (2023). A robust and efficient microvascular isolation method for multimodal characterization of the mouse brain vasculature. Cell Reports Methods *3*, 100431.

36. Kalucka, J., de Rooij, L.P.M.H., Goveia, J., Rohlenova, K., Dumas, S.J., Meta, E., Conchinha, N.V., Taverna, F., Teuwen, L.A., Veys, K., et al. (2020). Single-Cell Transcriptome Atlas of Murine Endothelial Cells. Cell *180*, 764–779.e20. https://doi.org/10.1016/j.cell.2020.01.015.

37. Dani, N., Herbst, R.H., McCabe, C., Green, G.S., Kaiser, K., Head, J.P., Cui, J., Shipley, F.B., Jang, A., Dionne, D., et al. (2021). A cellular and spatial map of the choroid plexus across brain ventricles and ages. Cell *184*, 3056–3074.e21. https://doi.org/10.1016/j.cell.2021.04.003.

38. del Toro, R., Prahst, C., Mathivet, T., Siegfried, G., Kaminker, J.S., Larrivee, B., Breant, C., Duarte, A., Takakura, N., Fukamizu, A., et al. (2010). Identification and functional analysis of endothelial tip cell-enriched genes. Blood *116*, 4025–4033. https://doi.org/10.1182/blood-2010-02-270819.

39. Fan, Z., Ardicoglu, R., Batavia, A.A., Rust, R., von Ziegler, L., Waag, R., Zhang, J., Desgeorges, T., Sturman, O., Dang, H.R., et al. (2023). The vascular gene Apold1 is dispensable for normal development but controls angiogenesis under pathological conditions. Angiogenesis *26*, 385–407. https://doi.org/10.1007/s10456-023-09870-z.

40. Poniatowski, Ł.A., Wojdasiewicz, P., Krawczyk, M., Szukiewicz, D., Gasik, R., Kubaszewski, Ł., and Kurkowska-Jastrzębska, I. (2017). Analysis of the Role of CX3CL1 (Fractalkine) and Its Receptor CX3CR1 in Traumatic Brain and Spinal Cord Injury: Insight into Recent Advances in Actions of Neurochemokine Agents. Mol. Neurobiol. *54*, 2167–2188. https://doi.org/10.1007/s12035-016-9787-4.

41. Butovsky, O., and Weiner, H.L. (2018). Microglial signatures and their role in health and disease. Nat. Rev. Neurosci. *19*, 622–635. https://doi.org/10.1038/s41583-018-0057-5.

42. Alvarez, J.I., Saint-Laurent, O., Godschalk, A., Terouz, S., Briels, C., Larouche, S., Bourbonnière, L., Larochelle, C., and Prat, A. (2015). Focal disturbances in the blood-brain barrier are associated with formation of neuroinflammatory lesions. Neurobiol. Dis. *74*, 14–24. https://doi.org/10.1016/j.nbd.2014.09.016.

43. Bowman, G.L., Kaye, J.A., Moore, M., Waichunas, D., Carlson, N.E., and Quinn, J.F. (2007). Blood-brain barrier impairment in Alzheimer disease: stability and functional significance. Neurology *68*, 1809–1814. https://doi.org/10.1212/01.wnl.0000262031.18018.1a.

44. Gray, M.T., and Woulfe, J.M. (2015). Striatal blood-brain barrier permeability in Parkinson's disease. J. Cereb. Blood Flow Metab. *35*, 747–750. https://doi.org/10.1038/jcbfm.2015.32.

45. Kettenmann, H., Hanisch, U.K., Noda, M., and Verkhratsky, A. (2011). Physiology of microglia. Physiol. Rev. *91*, 461–553. https://doi.org/10.1152/physrev.00011.2010.

46. Merlini, M., Rafalski, V.A., Rios Coronado, P.E., Gill, T.M., Ellisman, M., Muthukumar, G., Subramanian, K.S., Ryu, J.K., Syme, C.A., Davalos, D., et al. (2019). Fibrinogen Induces Microglia-Mediated Spine Elimination and Cognitive Impairment in an Alzheimer's Disease Model. Neuron *101*, 1099–1108.e6. https://doi.org/10.1016/j.neuron.2019.01.014.

47. Shan, Y., Tan, S., Lin, Y., Liao, S., Zhang, B., Chen, X., Wang, J., Deng, Z., Zeng, Q., Zhang, L., et al. (2019). The glucagon-like peptide-1 receptor agonist reduces inflammation and blood-brain barrier breakdown in an astrocyte-dependent manner in experimental stroke. J. Neuroinflammation *16*, 242. https://doi.org/10.1186/s12974-019-1638-6.

48. Ensoli, F., Fiorelli, V., Lugaresi, A., Farina, D., De Cristofaro, M., Collacchi, B., Muratori, D.S., Scala, E., Di Gioacchino, M., Paganelli, R., and Aiuti, F. (2002). Lymphomononuclear cells from multiple sclerosis patients spontaneously produce high levels of oncostatin M, tumor necrosis factors alpha and beta, and interferon gamma. Mult. Scler. *8*, 284–288. https://doi.org/10.1191/1352458502ms817oa.

49. Chapouly, C., Tadesse Argaw, A., Horng, S., Castro, K., Zhang, J., Asp, L., Loo, H., Laitman, B.M., Mariani, J.N., Straus Farber, R., et al. (2015). Astrocytic TYMP and VEGFA drive blood-brain barrier opening in inflammatory central nervous system lesions. Brain *138*, 1548–1567. https://doi.org/10.1093/brain/awv077.

50. Tomkins, O., Shelef, I., Kaizerman, I., Eliushin, A., Afawi, Z., Misk, A., Gidon, M., Cohen, A., Zumsteg, D., and Friedman, A. (2008). Blood-brain barrier disruption in post-traumatic epilepsy. J. Neurol. Neurosurg. Psychiatry *79*, 774–777. https://doi.org/10.1136/jnnp.2007.126425.

51. Friedman, A. (2011). Blood-brain barrier dysfunction, status epilepticus, seizures, and epilepsy: a puzzle of a chicken and egg? Epilepsia *52*, 19–20. https://doi.org/10.1111/j.1528-1167.2011.03227.x.

52. Schoknecht, K., Prager, O., Vazana, U., Kamintsky, L., Harhausen, D., Zille, M., Figge, L., Chassidim, Y., Schellenberger, E., Kovács, R., et al. (2014). Monitoring stroke progression: in vivo imaging of cortical perfusion, blood-brain barrier permeability and cellular damage in the rat photothrombosis model. J. Cereb. Blood Flow Metab. *34*, 1791–1801. https://doi.org/10.1038/jcbfm.2014.147.

53. Mayne, K., White, J.A., McMurran, C.E., Rivera, F.J., and de la Fuente, A.G. (2020). Aging and Neurodegenerative Disease: Is the Adaptive Immune System a Friend or Foe? Front. Aging Neurosci. *12*, 572090. https://doi.org/10.3389/fnagi.2020.572090.

54. Scharpfenecker, M., Fiedler, U., Reiss, Y., and Augustin, H.G. (2005). The Tie-2 ligand angiopoietin-2 destabilizes quiescent endothelium through an internal autocrine loop mechanism. J. Cell Sci. *118*, 771–780. https://doi.org/10.1242/jcs.01653.

55. Benest, A.V., Kruse, K., Savant, S., Thomas, M., Laib, A.M., Loos, E.K., Fiedler, U., and Augustin, H.G. (2013). Angiopoietin-2 is critical for cytokine-induced vascular leakage. PLoS One *8*, e70459. https://doi.org/10.1371/journal.pone.0070459.

56. Rathnakumar, K., Savant, S., Giri, H., Ghosh, A., Fisslthaler, B., Fleming, I., Ram, U., Bera, A.K., Augustin, H.G., and Dixit, M. (2016). Angiopoietin-2 mediates thrombin-induced monocyte adhesion and endothelial permeability. J. Thromb. Haemost. *14*, 1655–1667. https://doi.org/10.1111/jth.13376.

57. Kenig-Kozlovsky, Y., Scott, R.P., Onay, T., Carota, I.A., Thomson, B.R., Gil, H.J., Ramirez, V., Yamaguchi, S., Tanna, C.E., Heinen, S., et al. (2018). Ascending Vasa Recta Are Angiopoietin/Tie2-Dependent Lymphatic-Like Vessels. J. Am. Soc. Nephrol. *29*, 1097–1107. https://doi.org/10.1681/ASN.2017090962.

58. Souma, T., Thomson, B.R., Heinen, S., Carota, I.A., Yamaguchi, S., Onay, T., Liu, P., Ghosh, A.K., Li, C., Eremina, V., et al. (2018). Context-dependent functions of angiopoietin 2 are determined by the endothelial phosphatase VEPTP. Proc. Natl. Acad. Sci. USA *115*, 1298–1303. https://doi.org/10.1073/pnas.1714446115.

59. Keaney, J., Walsh, D.M., O'Malley, T., Hudson, N., Crosbie, D.E., Loftus, T., Sheehan, F., McDaid, J., Humphries, M.M., Callanan, J.J., et al. (2015). Autoregulated paracellular clearance of amyloid-beta across the blood-brain barrier. Sci. Adv. *1*, e1500472. https://doi.org/10.1126/sciadv.1500472.

60. Campbell, M., Hanrahan, F., Gobbo, O.L., Kelly, M.E., Kiang, A.S., Humphries, M.M., Nguyen, A.T.H., Ozaki, E., Keaney, J., Blau, C.W., et al. (2012). Targeted suppression of claudin-5 decreases cerebral oedema and improves cognitive outcome following traumatic brain injury. Nat. Commun. *3*, 849. https://doi.org/10.1038/ncomms1852.

61. Greene, C., and Campbell, M. (2016). Tight junction modulation of the blood brain barrier: CNS delivery of small molecules. Tissue Barriers *4*, e1138017. https://doi.org/10.1080/21688370.2015.1138017.

62. Dithmer, S., Staat, C., Müller, C., Ku, M.C., Pohlmann, A., Niendorf, T., Gehne, N., Fallier-Becker, P., Kittel, Á., Walter, F.R., et al. (2017). Claudin peptidomimetics modulate tissue barriers for enhanced drug delivery. Ann. N. Y. Acad. Sci. *1397*, 169–184. https://doi.org/10.1111/nyas.13359.

63. Mihajlica, N., Betsholtz, C., and Hammarlund-Udenaes, M. (2018). Pharmacokinetics of pericyte involvement in small-molecular drug transport across the blood-brain barrier. Eur. J. Pharm. Sci. *122*, 77–84. https://doi.org/10.1016/j.ejps.2018.06.018.

64. Lallemand, Y., Luria, V., Haffner-Krausz, R., and Lonai, P. (1998). Maternally expressed PGK-Cre transgene as a tool for early and uniform activation of the Cre site-specific recombinase. Transgenic Res. *7*, 105–112. https://doi.org/10.1023/a:1008868325009.

65. Hao, Y., Hao, S., Andersen-Nissen, E., Mauck, W.M., 3rd, Zheng, S., Butler, A., Lee, M.J., Wilk, A.J., Darby, C., Zager, M., et al. (2021). Integrated analysis of multimodal single-cell data. Cell *184*, 3573–3587.e29. https://doi.org/10.1016/j.cell.2021.04.048.

66. Wu, T., Hu, E., Xu, S., Chen, M., Guo, P., Dai, Z., Feng, T., Zhou, L., Tang, W., Zhan, L., et al. (2021). clusterProfiler 4.0: A universal enrichment tool for interpreting omics data. Innovation *2*, 100141. https://doi.org/10.1016/j.xinn.2021.100141.

67. Love, M.I., Huber, W., and Anders, S. (2014). Moderated estimation of fold change and dispersion for RNA-seq data with DESeq2. Genome Biol. *15*, 550. https://doi.org/10.1186/s13059-014-0550-8.

68. Percie du Sert, N., Hurst, V., Ahluwalia, A., Alam, S., Avey, M.T., Baker, M., Browne, W.J., Clark, A., Cuthill, I.C., Dirnagl, U., et al. (2020). The ARRIVE guidelines 2.0: Updated guidelines for reporting animal research. J. Cereb. Blood Flow Metab. *40*, 1769–1777. https://doi.org/10.1177/0271678X20943823.

69. Vazquez-Liebanas, E., Nahar, K., Bertuzzi, G., Keller, A., Betsholtz, C., and Mäe, M.A. (2022). Adult-induced genetic ablation distinguishes PDGFB roles in blood-brain barrier maintenance and development. J. Cereb. Blood Flow Metab. *42*, 264–279. https://doi.org/10.1177/0271678X211056395.

70. Vanlandewijck, M., Lebouvier, T., Andaloussi Mäe, M., Nahar, K., Hornemann, S., Kenkel, D., Cunha, S.I., Lennartsson, J., Boss, A., Heldin, C.H., et al. (2015). Functional Characterization of Germline Mutations in PDGFB and PDGFRB in Primary Familial Brain Calcification. PLoS One *10*, e0143407. https://doi.org/10.1371/journal.pone.0143407.

71. Becht, E., McInnes, L., Healy, J., Dutertre, C.A., Kwok, I.W.H., Ng, L.G., Ginhoux, F., and Newell, E.W. (2018). Dimensionality reduction for visualizing single-cell data using UMAP. Nat. Biotechnol. *37*, 38–44. https://doi.org/10.1038/nbt.4314.

72. Kim, D., Pertea, G., Trapnell, C., Pimentel, H., Kelley, R., and Salzberg, S.L. (2013). TopHat2: accurate alignment of transcriptomes in the presence of insertions, deletions and gene fusions. Genome Biol. *14*, R36. https://doi.org/10.1186/gb-2013-14-4-r36.

73. Langmead, B., and Salzberg, S.L. (2012). Fast gapped-read alignment with Bowtie 2. Nat. Methods *9*, 357–359. https://doi.org/10.1038/nmeth.1923.

STAR★METHODS

KEY RESOURCES TABLE

REAGENT or RESOURCE	SOURCE	IDENTIFIER
Antibodies		
ACTA2-Cy3 (1:100)	Sigma Aldrich	Cat. #C6198; RRID:AB_476856
ACTA2-Alexa Fluor 647 (1:100)	Santa Cruz	Cat. #Sc-32251; RRID:AB_262054
ACTB (1:500)	Cell Signaling Technology	Cat. #4967L; RRID:AB_330288
ANGPT2 (1:200)	From Prof. Gou Young Koh	N/A
CD45 (1:100)	BD Biosciences	Cat. #550539; RRID:AB_2174426
CLDN5 (IF 1:100, WB 1:500)	ThermoFischer Scientific	Cat. #34–1600; RRID:AB_2533157
DECTIN1 (1:100)	Invivogen	Cat. #mabg-mdect; RRID:AB_2753143
ERG (1:200)	Abcam	Cat. #Ab92513; RRID:AB_2630401
GFAP (1:100)	Zymed labs	Cat. #13–0300; RRID:AB_2532994
GFP (for EYFP) (1:300)	Abcam	Cat. #ab13970; RRID:AB_300798
Histone H3 (1:1000)	Cell Signaling Technology	Cat. #4620; RRID:AB_1904005
IBA1 (1:100)	FUJIFILM Wako Shibayagi	Cat. #019–19741; RRID:AB_839504
IBA1 (1:100)	Abcam	Cat. #ab5076; RRID:AB_2224402
ICAM1 (1:100)	Abcam	Cat. #ab25375; RRID:AB_470490
NEUN (1:100)	Chemicon	Cat. #Mab377; RRID:AB_2298772
OCLN (1:100)	ThermoFischer Scientific	Cat. #71–1500; RRID:AB_2533977
PECAM1 (1:200)	R&D Systems	Cat. #AF3628; RRID:AB_2161028
PECAM1 (1:200)	BD Biosciences	Cat. #553370; RRID:AB_394816
SLC16A1 (1:100)	Acris	Cat. #TA321556; RRID N/A
VE-Cadherin (1:200)	eBioscience	Cat. #14144181; RRID:AB_842768
ZO-1 (1:100)	ThermoFischer Scientific	Cat. #40–2300; RRID:AB_2533457
Anti-goat DyLight 405 (1:600)	Jackson ImmunoResearch	Cat. #705-475-147; RRID:AB_2340427
Anti-goat Alexa Fluor 488 (1:600)	Jackson ImmunoResearch	Cat. #705-546-147; RRID: AB_2340430
Anti-goat Cy3 (1:600)	Jackson ImmunoResearch	Cat. #705-165-003; RRID:AB_2340411
Anti-goat CF 633 (1:600)	Merck	Cat. #SAB4600128; RRID N/A
Anti-goat Alexa Fluor 647 (1:600)	Jackson ImmunoResearch	Cat. #705-605-147; RRID:AB_2340437
Anti-goat Alexa Fluor Plus 680 (1:600)	ThermoFischer Scientific	Cat. #A32860; RRID:AB_2762841
Anti-rat Alexa Fluor 488 (1:600)	Jackson ImmunoResearch	Cat. #712-546-153; RRID:AB_2340686
Anti-rat Cy3 (1:600)	Jackson ImmunoResearch	Cat. #712-165-150; RRID:AB_2340666
Anti-rat Alexa Fluor Plus 555 (1:600)	ThermoFischer Scientific	Cat. #A48270; RRID:AB_2896336
Anti-rat CF 633 (1:600)	Merck	Cat. #SAB4600133; RRID N/A
Anti-rat Alexa Fluor 647 (1:600)	Jackson ImmunoResearch	Cat. #712-605-153; RRID:AB_2340694
Anti-rat Alexa Fluor 680 (1:600)	ThermoFischer Scientific	Cat. #712-625-153; RRID:AB_2340699
Anti-rabbit Alexa Fluor 488 (1:600)	Jackson ImmunoResearch	Cat. #711-546-152; RRID:AB_2340619
Anti-rabbit Alexa Fluor Plus 488 (1:600)	ThermoFischer Scientific	Cat. #A32790TR; RRID:AB_2866495
Anti-rabbit Cy3 (1:600)	Jackson ImmunoResearch	Cat. #711-166-152; RRID:AB_2313568
Anti-rabbit CF 633 (1:600)	Merck	Cat. #SAB4600132; RRID N/A
Anti-rabbit Alexa Fluor 647 (1:600)	Jackson ImmunoResearch	Cat. #711-605-152; RRID:AB_2492288
Anti-rabbit IgG, HRP-linked (1:2500)	Cell Signaling Technology	Cat. #7074; RRID:AB_2099233
Anti-chicken Alexa Fluor 488 (1:600)	Jackson ImmunoResearch	Cat. #703-545-155; RRID:AB_2340375
Anti-chicken Cy3 (1:600)	Jackson ImmunoResearch	Cat. #703-165-155; RRID:AB_2340363
Anti-chicken Alexa Fluor 647 (1:600)	Jackson ImmunoResearch	Cat. #703-605-155; RRID:AB_2340379

(*Continued on next page*)

Continued

REAGENT or RESOURCE	SOURCE	IDENTIFIER
Anti-human Alexa Fluor 488 (1:600)	Jackson ImmunoResearch	Cat. #709-545-149; RRID:AB_2340566
Anti-human Cy3 (1:600)	Jackson ImmunoResearch	Cat. #709-165-149; RRID:AB_2340535
Anti-human Alexa Fluor 647 (1:600)	Jackson ImmunoResearch	Cat. #709-605-098; RRID:AB_2340577
Anti-human Alexa Fluor 647 (1:600)	Jackson ImmunoResearch	Cat. #709-605-149; RRID:AB_2340578
Chemicals, peptides, and recombinant proteins		
Hoechst 33342	Thermo Fischer Scientific	Cat. #H3570
1 kDa Alexa Fluor 555 Cadaverine	Life Technologies	Cat. #A30677
3 kDa TMR-Dextran	Thermo Fisher Scientific	Cat. #D3308
10 kDa TMR-Dextran	Thermo Fisher Scientific	Cat. #D1817
70 kDa TMR-Dextran	Thermo Fisher Scientific	Cat. #D1818
Evans blue dye	Thermo Fisher Scientific	Cat. #E2129
Lipofectamine 2000	Invitrogen	Cat. #11668027
RIPA Lysis and Extraction Buffer	Thermo Fisher Scientific	Cat. #89901
Normal donkey serum	Jackson ImmunoResearch	Cat. #017-000-121
Prolong Gold anti-fade reagent	Thermo Fischer Scientific	Cat. #P36930
Triton X-100	Sigma-Aldrich	Cat. #T8787
TrypLE	Gibco	Cat. #A1217701
Collagenase type II	Sigma-Aldrich	Cat. #C6885
Collagenase IV	Gibco	Cat. #17104-019
Sheep anti-rat magnetic Dynabeads®	Invitrogen	Cat. #11035
Tamoxifen	Sigma-Aldrich	Cat. #T5648
cOmplete™ Protease Inhibitor Cocktail	Sigma-Aldrich	Cat. #4693116001
DMEM GlutaMAX	Gibco	Cat. #31966021
Peanut oil	Sigma-Aldrich	Cat. #C8267
Critical commercial assays		
Chromium Next GEM Single Cell 3′ GEM, Library &Gel Bead Kit v3.1 16 rxns	10x Genomics	Cat. #1000121
Chromium Next GEM Chip G Single Cell Kit, 48 rxns	10x Genomics	Cat. #1000120
iScript™ Reverse Transcription Supermix	Bio-Rad	Cat. #1708840
Cytiva Amersham™ ECL™ detection kit	Thermo Fisher Scientific	Cat. #10308449
Super Signal West Femto kit	Thermo Fisher Scientific	Cat. #34095
Deposited data		
Raw sequencing reads and processed gene expression counts	This paper	GEO: GSE250382
Online database	This paper	https://sicof.medh.ki.se/cldn5/EC
Experimental models: Cell lines		
Mouse brain endothelial cells (bEnd.3)	ATCC	Cat. #CRL-2299, LOT #70030469
Experimental models: Organisms/strains		
Mouse: *Gt(ROSA)26Sor*$^{tm1(EYFP)Cos}$*/J*	Srinivas et al.[28] The Jackson Laboratory	stock #006148
Mouse: Tg(*Cdh5*-CreERT2)1Rha	Pitulescu et al.[27]	N/A
Mouse: Tg(*Pgk1*-Cre) mice	Lallemand et al.[64]	N/A
Mouse: *Cldn5*-tm(Flox)	This paper	N/A
Oligonucleotides		
non-targeting control siRNA: siCtrl	Ambion	Cat. #AM4636
Cldn5-targeting siRNA: si*Cldn5*	Dharmacon	Cat. #D-042358-04-0050
Cldn5-VIC	Thermo Fisher Scientific	Mm00727012_s1
Cdh5-FAM	Thermo Fisher Scientific	Mm00486938_m1

(*Continued on next page*)

Continued

REAGENT or RESOURCE	SOURCE	IDENTIFIER
Actb-FAM	Thermo Fisher Scientific	Mm00607939_s1
Kdr-FAM	Thermo Fisher Scientific	Mm01222421_m1
Gapdh-Cy5.5	Bio-Rad	qMmuCEP0039581
Software and algorithms		
Graph Pad Prism v 9	GraphPad Software	https://www.graphpad.com
ImageJ v 1.53c	Wayne Rasband (National Institutes of Health)	http://imagej-nih.gov/ij
Illustrator v 27.5	Adobe	https://www.adobe.com/products/illustrator.html
Photoshop v 25.1.0	Adobe	https://www.adobe.com/products/photoshop.html
ImageLab v 5.2.1	Bio-Rad	https://www.biorad.com/ense/product/image-labsoftware?ID = KRE6P5E8Z
Seurat v4.0.1 package for R	Hao et al.[65]	RRID:SCR_007322; https://satijalab.org/seurat/articles/install.html
Cell Ranger v 7	10X Genomics	https://support.10xgenomics.com/single-cell-geneexpression/software/downloads/latest
clusterProfiler	Guangchuang et al.[66]	RRID:SCR_016884; http://bioconductor.org/packages/release/bioc/html/clusterProfiler.html
DEseq2	Love et al.[67]	RRID:SCR_015687; https://bioconductor.org/packages/release/bioc/html/DESeq2.html
Other		
Leica M205 FA	Leica Microsystems	https://www.leica-microsystems.com/
Leica TCS SP8 confocal	Leica Microsystems	https://www.leica-microsystems.com/
ChemiDoc™ MP gel imaging system	BioRad	https://www.bio-rad.com/en-se/product/chemidoc-xrs-system?ID=NINJHRKG4
Synergy HT microplate reader	BioTek	
NextSeq2000	Illumina	Cat. #20040559
LUNA-FI™ cell counter	Logos	Cat. #L20001
AO/PI cell viability kit	Logos	Cat. #F23001

RESOURCE AVAILABILITY

Lead contact

Further information and requests for resources and reagents should be directed to and will be fulfilled by the Lead Contact, Maarja Andaloussi Mäe (maarja.andaloussi_mae@igp.uu.se).

Materials availability

Mouse line generated in this study is available from the lead contact upon request.

Data and code availability

- Single-cell RNA-seq data have been deposited at GEO and are publicly available as of the date of publication. Accession number is listed in the key resources table. Online searchable databases of annotated gene expression data are described in the key resources table.
- This paper does not report original code.
- All data and additional information required to re-analyze the data reported in this paper are available from the lead contact upon request.

EXPERIMENTAL MODEL AND STUDY PARTICIPANT DETAILS

Experimental mice

Endothelial-specific tamoxifen-inducible *Cldn5* knock-out mice (*Cldn5*^{iECKO}) were obtained crossing the endothelial specific *Cdh5*(PAC)-Cre^{ERT2} mice[27] with *Cldn5*$^{flox/flox}$ mice (Taconic, UPP0053 Cldn5). The conditional floxed *Cldn5* allele was achieved

via homologous recombination in the Taconic Biosciences C57BL/6NTac embryonic stem cell line. The homologous recombinant clones were selected via positive selection for puromycin resistance (PuroR) and negative selection of thymidine kinase. The PuroR selection marker was flanked with flippase recognition target (FRT) sites and after selection PuroR was eliminated with Flippase (Flp) *in vivo*. A schematic representation of the generation of the conditional floxed *Cldn5* allele can be seen in Figure S1A. To evaluate Cre recombination efficiency, the animals were crossed with *Rosa26*$^{EYFP/YFP}$ reporter mice (www.jax.org, stock #006148). All mice were of mixed background: C57BL/6J (Jackson Laboratory), C57BL/6N (Charles River Laboratory) and 129X1/SvJ (Jackson Laboratory). In all the experiments, Cre-negative *Cldn5*$^{flox/flox}$ littermate mice were referred to as Controls (Ctrl). In all analyzed mice, *Cldn5* deletion was achieved through oral gavage of 100 μL of a 20 mg/mL Tamoxifen (cat. #T5648, Sigma-Aldrich) solution in 90% peanut oil (cat. #C8267, Sigma-Aldrich) and 10% ethanol for 3 consecutive days at around 3 months of age. Both male and female mice were used for the analyses. The mice were sacrificed for analysis 3-15 days after first dose of Tamoxifen induction.

Constitutive *Cldn5* heterozygous (*Cldn5*$^{+/-}$) mice were obtained crossing the *Pgk1*-Cre mice[64] with *Cldn5*$^{flox/+}$ mice. Mice were back-crossed at least 5 generations to C57BL/6J background.

All animal experiment protocols were approved by the Uppsala Ethical Committee on Animal Research (permit numbers C115/15, C111515/16, 5.8.18–03029/2020) and were carried out in accordance with their guidelines. Experiments have been reported in compliance with the ARRIVE 2.0 guidelines.[68] All efforts were made to minimize animal suffering. Both male and female mice were used in the experiments, and the studied phenotypes did not differ between sexes. No animals were excluded from the analyses. All quantifications were carried out with the investigator blinded to genotype.

METHOD DETAILS

Microvascular fragment isolation for quantitative PCR (qPCR), western blot and scRNAseq

11 days after first dose of tamoxifen induction, the following mice were anesthetized with 50 mg/mL Ketamin (Ketaminol, Intervet) and 20 mg/mL Xylasin (Rompun, Bayer) in Phosphate Buffered Saline (PBS, cat. #12-9423-5, Medicago) and sacrificed through cervical dislocation: at 11–13 dpi for qPCR (11 dpi: Ctrl n = 4, *Cldn5*^{iECKO} n = 3, 12 dpi: Ctrl n = 2, *Cldn5*^{iECKO} n = 3 and 13 dpi: Ctrl n = 2, *Cldn5*^{iECKO} n = 3) and at 11 dpi for scRNAseq (Ctrl male n = 2, female n = 1, *Cldn5*^{iECKO} male n = 2, female n = 1, 3 independent experiments). For Western blot (n = 6, 2 independent experiments), the adult mice were anesthetized as stated above and sacrificed through cervical dislocation.

For qPCR, the cerebrum was collected and split in two-halves and the microvascular fragments (MVF) were isolated from each half as previously described.[69]

For Western blot and scRNAseq, the cerebrums were collected and the MVFs were isolated as previously described[35] with minor modifications prior 10x Genomics scRNAseq. In brief, the brain halves were mechanically and enzymatically digested with Collagenase type II (1 mg/mL, cat. #C6885, Sigma). On ice, the washed MVFs were isolated using sheep anti-rat magnetic Dynabeads (50 μL/brain, cat. #11035, Invitrogen) bound to rat anti-mouse PECAM1 antibody (10 μL/brain, cat. #553370, BD Biosciences) and a DynaMag 2 magnet (Invitrogen). The washed MVFs were then further dissociated with Collagenase IV (1 mg/mL, cat. #17104-019, Gibco) and TrypLE (cat. #A1217701, Gibco) to remove the magnetic beads and obtain single cell solutions.

qPCR

The MVFs were lysed in RLT buffer and the RNA was extracted using the RNeasy micro prep kit according to the manufacturer's protocol (cat. #74034, Qiagen). iScript Reverse Transcription Supermix (cat. #1708840, Bio-Rad) was used to synthesize cDNA and mRNA expression was quantified by TaqMan assays from 24 ng of cDNA per mouse. The measured *Cldn5* expression levels were normalized to endogenous gene expression levels of *Gapdh* for each mouse. The specific probes used are listed in the key resources table. Two litters of were used for this analysis at 11–13 dpi (11 dpi: Ctrl n = 4, *Cldn5*^{iECKO} n = 3, 12 dpi: Ctrl n = 2, *Cldn5*^{iECKO} n = 3 and 13 dpi: Ctrl n = 2, *Cldn5*^{iECKO} n = 3).

Similarly, MVF from the cerebrum of adult *Cldn5* heterozygous and homozygous littermate control mice were isolated. *Cldn5* mRNA expression was quantified by TaqMan assays from 24 ng of cDNA per mouse. The measured expression levels were normalized to endogenous gene expression of *Actb* for each mouse as well as *Cdh5* and *Kdr*. Two litters were used for this analysis, *Cldn5*$^{+/+}$ n = 5, *Cldn5*$^{+/-}$ n = 6.

Western blot

The cells from MVFs were lysed with 100 μL ice-cold RIPA Lysis and Extraction Buffer (cat. #89901, Thermo Fisher Scientific) supplemented with 1X Roche cOmplete Protease Inhibitor Cocktail (cat. #4693116001, Sigma-Aldrich). The lysates were then frozen and thawed for two times and incubated at 4°C for 2 h in a rotator.

The protein lysates were quantified using the Pierce BCA kit (cat. #23225, Thermo Fisher Scientific) and, equal amounts (0.7 μg) of protein were loaded and electrophoresed using NuPAGE 4 to 12%, Bis-Tris, 1.0–1.5 mm, Mini Protein Gels (cat. #NP0323BOX, Thermo Fisher Scientific). The proteins were then transferred using Trans-Blot Turbo transfer system (cat. #1704156, BioRad) at 1.3 A and 25 V for 7 min. The membrane was then blocked with 5% BSA in 20 mM Tris base, 135 mM NaCl, 0.1% Tween 20 (TBST) for 30 min at RT. The membrane was incubated with the primary antibody for 1.5 h at RT washed three times with TBST and, the bound antibodies were detected using horseradish peroxide conjugated secondary antibodies incubated for 1 h at RT

followed by washes with TBST for four times. After incubation with the substrate – Cytiva Amersham ECL detection kit (cat. #10308449, Thermo Fisher Scientific) or Super Signal West Femto kit (cat. #34095, Thermo Fisher Scientific) – HRP-stained bands were detected with the ChemiDoc gel imaging system (BioRad).

BBB permeability

The assessment of the BBB permeability was performed as previously described.[33] Briefly, different molecular size fluorescent tracers were administered intravenously into the tail vein. The information about the tracers, circulation times and number of mice used are included in Table S1. After anesthesia, the mice were perfused with Hank's Balanced Salt Solution (HBSS, cat. #14025092, Life Technologies) for 3–4 min. One-half of the brain and one kidney were homogenized in 1% Triton X-100/PBS, pH 7.2. The lysates were centrifuged at 16,900 g for 20 min and the relative fluorescence of the supernatant was measured on a Synergy HT microplate reader (BioTek) with the following filters: excitation 540/25 nm, emission 590/20 nm. The relative fluorescence of Evans Blue Dye (EBD) was measured with the following filters: excitation 620/15 nm, emission 680/30 nm. To ensure the systemic distribution of the tracers, kidneys were used as a control. The relative fluorescence units per tissue weight (RFU/g) was calculated and the results are presented as the fold change of the Ctrl, which is set to 1. Also, whole brain and kidney fluorescent images were taken with Leica M205 FA stereomicroscope.

Immunofluorescence stainings

After full anesthesia, the mice were perfused transcardially with HBSS and 4% buffered formaldehyde (formalin, cat. #2178, Histolab). Brains were collected and post-fixed in 4% formalin for 4 h at 4°C and sliced into 75 μm-thick sagittal sections. The mice used for OCLN and ZO1 stainings were perfused with HBSS and 1% formalin and the brains were collected and incubated in ice-cold 100% methanol overnight at 4°C and sliced into 75 μm-thick sections after gradual rehydration (75%, 50%, 25%, 0% methanol, each step 20 min at 4°C). All sections were incubated in permeabilization and blocking buffer (1% bovine serum albumin (BSA), 5% normal donkey serum (cat. #017-000-121, Jackson ImmunoResearch) and 0.75% Triton X-100 (cat. #T8787, Sigma-Aldrich) in PBS) overnight at 4°C. Primary antibodies (diluted in 0.5% BSA, 0.25% Triton X-100 in PBS) were incubated 48 h at 4°C, followed by an overnight-secondary antibody incubation at 4°C. Nuclei was stained with Hoechst 33342 (cat. #H3570, Thermo Fischer Scientific). The stained sections were mounted in Prolong Gold anti-fade reagent (cat. #P36930, Thermo Fischer Scientific). All images were taken with a Leica TCS SP8 confocal microscope (Leica Microsystems), and are shown in the figures as maximum intensity projections of z-stacks. Image analysis was done using Fiji (ImageJ), image brightness levels and sizing was adjusted using Adobe Photoshop v25.1.0 and figures were built using Adobe Illustrator v27.5.

EYFP longitudinal recombination and CLDN5 longitudinal expression analysis in cerebral cortex

To assess the percentage of EYFP recombination in the capillary endothelium of the mouse brain cortex, EYFP+ capillary length was manually measured using Fiji as well as the total capillary length per field (PECAM1+ length). Vessels were considered capillaries if they were smaller than approximately 6 μm in diameter. The percentage of EYFP capillary recombination was then calculated as the percentage of EYFP+ capillary length/PECAM1+ length. In a similar way, the CLDN5 longitudinal capillary expression in the endothelium was calculated as the CLDN5+ capillary length per field and normalized by the total PECAM1+ capillary length per field. For both measurements, ten fields per mouse brain cortex were analyzed. The mice were used at 11 dpi (four litters, Ctrl = 12, *Cldn5*^{iECKO} n = 13), 14 dpi (n = 3) and severe litter (15 dpi, Ctrl = 2, *Cldn5*^{iECKO} n = 3).

Endothelial cell quantification in cerebral cortex

The capillary length was measured using the AnalyzeSkeleton plug-in in Fiji as previously reported.[70] The total skeletal length was measured for PECAM1+ staining per each field taken from the brain cortex. If any bigger vessels were included in the field they were measured manually and excluded from the total skeletal length measurement per field. Vessels were considered capillaries if they were smaller than approximately 6 μm in diameter assessed by eye. The number of capillary endothelial cells per field (#capillary EC/field) was counted from ERG staining. The number of ERG+ cells per 100 μm of capillary length was also calculated (100*(ERG+ cells/PECAM1+ capillary length)). For each mouse brain cortex, ten fields were analyzed and the average per field is shown in the results. Two litters were used at 11 dpi (Ctrl = 10, *Cldn5*^{iECKO} n = 9) and severe litter (15 dpi, Ctrl = 2, *Cldn5*^{iECKO} n = 3).

EYFP longitudinal recombination and CLDN5 longitudinal expression analysis in cerebral cortex, hippocampus and thalamus – Comparative experiment

To assess the percentage of EYFP recombination in the capillary endothelium of the mouse brain cortex, hippocampus and thalamus, EYFP+ capillary length was manually measured using Fiji as well as the total capillary length per field (PECAM1+ length). Vessels were considered capillaries if they were smaller than approximately 6 μm in diameter. The percentage of EYFP capillary recombination was then calculated as the percentage of EYFP+ capillary length/PECAM1+ length. In a similar way, the CLDN5 longitudinal capillary expression in the endothelium was calculated as the CLDN5+ capillary length per field and normalized by the total PECAM1+ capillary length per field. For both measurements, ten fields per mouse brain cortex and hippocampus were analyzed, while minimum 6 fields per thalamus were analyzed. One litter was used at 11 dpi, Ctrl n = 3, *Cldn5*^{iECKO} n = 3.

MVF isolation and single-cell RNA sequencing using 10x genomics technology

The cells from MVFs from both halves were pooled and they were counted using a LUNA-FI (Logos) cell counter. Prior to sequencing, 5000 single cells per sample were captured in lipid droplets using Next Gem Single Cell 3′ Reagent kit v3.1. from 10x Genomics using manufacturer's instructions. The sequencing of full libraries was performed on the Illumina platform NextSeq2000 using the P3 reagent kit with a 100 cycles flow cell. The goal average read depth was 40000 reads/cell.

Bioinformatical analyses of single-cell RNA sequencing

The flow cell data were demultiplexed and aligned with the Cell Ranger pipeline (v6.1.2, 10x Genomics). After alignment, the combined data were analyzed with the Seurat package[65] in R with minor modifications. After quality control, genes expressed in less than 3 cells were considered absent, and cells with less than 500 total counts were filtered out of the dataset. Finally, libraries with high relative content ($\geq$10%) of mitochondrial genes were removed.

The 2000 most variable genes were used to calculate principal components of variation. Dimension reduction plots were visualized using the UMAP function (UMAP: uniform manifold approximation and projection).[71] The graph-based clustering approach with K-nearest neighbor (KNN) graph from the Seurat pipeline was used for clustering using principal component analysis (PCA) reduction in 30 dimensions at 0.8 resolution.

Cells belonging to clusters with high expression of typical endothelial cell markers (i.e., *Pecam1, Cldn5, Podxl* and *Cdh5*) were separately reanalyzed, using PCA reduction in 30 dimensions at 0.4 resolution. Cells with *Cldn5* counts equal to 0 and *Pecam1* counts over 0 were identified as cells with *Cldn5*$^{-}$ transcriptomes. Differential expressed genes were calculated using the Wilcoxon rank-sum test with average log2FC > 0.6 and p value adjusted <0.05 as parameters.

Data can be explored gene by gene on the online database: https://sicof.medh.ki.se/cldn5/EC/

Gene Ontology analyses

Gene ontology analysis was performed with the clusterProfiler R-software package.[66] The enrichGO function was applied to identify enriched GO terms belonging to the Biological Process subontology. Upregulated and downregulated DEGs of cluster 2 were compared with the list of all genes from EC dataset as reference. Terms with an adjusted p value <0.05 (pvalueCutoff = 0.05, pAdjustMethod = ''BH'' (BH = Benjamini-Hochberg)) were selected and to omit redundant terms, a cut-off 0.7 was used to simplify the function.

SLC16A1 longitudinal expression quantification and EYFP correlation in cerebral cortex

The percentage of SLC16A1 longitudinal capillary expression in the cerebral cortex was calculated via immunostaining of SLC16A1, ACTA2 and PECAM1. Additionally, EYFP was also stained to assess the correlation of SLC16A1 loss with EYFP recombination efficiency in the capillaries. Briefly, the ACTA2+ area was eliminated from the field to avoid considering arterioles (mostly SLC16A1-) in our quantifications. If any bigger veins (>6 μm in thickness, ACTA2- vessels) were present in the field, they were manually eliminated from the field. The length of SLC16A1 and EYFP stainings were measured using the AnalyzeSkeleton plug-in in Fiji, while the length of PECAM1 was measured manually in Fiji due to high background noise. From these initial measurements, the percentage of SLC16A1 longitudinal capillary expression was then quantified as 100*(SLC16A1+ length/PECAM1+ length). The EYFP recombination was quantified as 100*(EYFP+ length/PECAM1+ length). From the binary images of SLC16A1+ capillaries and EYFP+ capillaries, the overlap between the two images was calculated using the Image Calculator tool in Fiji. The length of this overlap was considered as the length of SLC16A1+ staining in EYFP+ capillaries, thus the percentage of SLC16A1+EYFP+ capillaries was calculated as 100*(SLC16A1 and EYFP overlap/EYFP+ length).

Potential correlation between %SLC16A1 longitudinal capillary expression and %EYFP recombination in the capillary was addressed computing two-tailed Pearson correlation coefficients with 95% confidence interval. For all measurements, ten fields per mouse brain cortex were analyzed. Two litters were used at 11 dpi, Ctrl n = 6, *Cldn5*^{iECKO} n = 8.

Cldn5 downregulation in bEnd.3 cell culture and RNAseq

To investigate potential cell-autonomous transcriptional changes of *Cldn5* loss *in vitro*, 6 × 10^{4} bEnd.3 cells 10% FBS DMEM GlutaMAX (cat. #31966021, Gibco) were seeded in a 96 well plate. When cells were approximately 70% confluent, cells were transfected with the siRNA (non-targeting control siRNA: siCtrl, cat. #AM4636, Ambion) or with *Cldn5*-targeting siRNA: si*Cldn5,* cat. #D-042358-04-0050, Dharmacon)) and Lipofectamine 2000 (cat. #11668027, Invitrogen) at different concentrations (0, 1, 10 or 40 pmol) and different treatment durations (6, 12, 24 or 48 h). The bulk of each well was lysed and prepared for sequencing with the SmartSeq2 technology and sequenced with the Illumina platform NextSeq2000 using the P3 reagent kit with a 100 cycles flow cell. The samples were aligned to the mouse reference genome GRCm38 (mm10) using TopHat2[72] with Bowtie2.[73] The resulting read counts were analyzed with a DEseq2 pipeline[67] with minor modifications. Genes with cumulative counts less than 30 counts were considered as background and were therefore removed. Differentially expressed genes were calculated with average log2FC > 0.6 and p value adjusted <0.05 as parameters.

ICAM1 longitudinal expression analysis in cerebral cortex

The ICAM1 longitudinal capillary expression in the brain cortex was manually measured using Fiji as the ICAM1+ capillary length per field normalized by the PECAM1+ capillary length per field. Vessels were considered capillaries if they were smaller than approximately 6 μm in diameter measured by eye. Ten fields per mouse brain cortex were analyzed. Three litters were used, one litter at 11 dpi (Ctrl n = 3, *Cldn5*^{iECKO} n = 2), one litter at 14 dpi (Ctrl n = 3, *Cldn5*^{iECKO} n = 3) and one severe litter (15 dpi, Ctrl n = 2, *Cldn5*^{iECKO} n = 3).

IBA1+ and CLEC7A + cell number quantification in cerebral cortex, thalamus and hippocampus

The total number of IBA1+ and CLEC7A + cell bodies per field was manually counted using Fiji and CLEC7A + cell numbers were normalized to the total number of IBA1+ cells per field. For cerebral cortex, 10 fields per mouse brain cortex were analyzed - two litters at 6 dpi (Ctrl n = 4, *Cldn5*^{iECKO} n = 5), two litters at 11 dpi (Ctrl n = 6, *Cldn5*^{iECKO} n = 6), two severe litters, one with observed seizures and one at 15 dpi (Ctrl n = 5, *Cldn5*^{iECKO} n = 7). For thalamus, 3 and for hippocampus, 4–6 pictures were analyzed, two litters at 11 dpi (Ctrl n = 7, *Cldn5*^{iECKO} n = 6) and two severe litters, one with observed seizures and one at 15 dpi (Ctrl n = 5, *Cldn5*^{iECKO} n = 7). For all quantifications, a fold change for each litter was calculated as the ratio of each mouse in relation to the average of the Ctrl.

QUANTIFICATION AND STATISTICAL ANALYSIS

All of the statistical details of experiments can be found in the figure legends, including the statistical tests used and exact value of analyzed mice (n). The data is shown as geometric mean ± geometric SD. If zero values were present, the data is shown as mean ± SD. To study normality, Shapiro-Wilk and Kolmogorov-Smirnov test were used. Normally-distributed two-group comparisons were tested for significance using the two-tailed, unpaired student's *t*-test. Not normally distributed two-group comparisons were tested for significance with the non-parametric Mann Whitney U test. $p \leq 0.05$ was considered statistically significant for all tests. Normally distributed multiple comparisons were tested for significance using the Tukey's multiple comparisons ANOVA test with alpha = 0.05. The group size was determined according to practical circumstances and no prior power calculations were performed. All the images included in the figures of this manuscript were selected because they were the most representative examples of each of the phenotypes.